PHYSICAL REVIEW E **111**, 045415 (2025)

Microscale structural fluctuations at the melting phase transition of strongly confined achiral and chiral nematics

J. Pišljar,[1,2,*] A. Nych,[3,1] U. Ognysta,[3] S. Kralj,[4,1] and I. Muševič[1,2]
[1]Condensed Matter Department, J. Stefan Institute, Jamova 39, 1000 Ljubljana, Slovenia
[2]Faculty of Mathematics and Physics, University of Ljubljana, Jadranska 19, 1000 Ljubljana, Slovenia
[3]Department of Molecular Photoelectronics, Institute of Physics, Nauky prospect 46, Kyiv 03680, Ukraine
[4]Department of Physics, Faculty of Natural Sciences and Mathematics, University of Maribor, Koroška 160, 2000 Maribor, Slovenia

(Received 30 October 2024; revised 6 March 2025; accepted 24 March 2025; published 15 April 2025)

We report on direct microscopic observations of thermally driven fluctuating dynamics in a narrow temperature region between the isotropic and low-temperature phases in achiral, chiral, and strongly chiral (blue phase) liquid crystal materials. We observe the dynamics in samples strongly confined between two glass surfaces which act as disordering surfaces at thicknesses above the critical confinement thickness below which the phase transition is gradual. In achiral and long-pitch chiral materials the fluctuating appears as formation and disappearance of small structureless nematic domains, whereas in strongly chiral materials, which exhibit blue phase I at larger thicknesses, these fluctuations are real-time formation and annihilation of topologically nontrivial nematic half-skyrmions. We study the dynamics of these fluctuations and present a simple model that explains how such dynamics is possible in ultraconfined systems.

DOI: 10.1103/PhysRevE.111.045415

I. INTRODUCTION

Confinement of liquids to nanoscale cavities or narrow gaps with dimensions of the order of a few or a few-tens of typical intermolecular distances has received special attention in physics due to the onset of capillary condensation, first described on thermodynamic grounds by Lord Kelvin [1] and since studied extensively, especially in water [2]. In liquid crystals (LCs), pioneering work on the confinement-induced condensation of the uniaxially ordered nematic phase (N) from the weakly ordered isotropic phase (referred to as the paranematic (P) phase in confinement) was conducted by Sheng [3,4]. He theoretically predicted that this phase transition, which is weakly first-order in bulk, would become continuous and gradual beyond a material- and surface-dependent critical point, (T_{cp}, d_c), where T_{cp} and d_c denote the critical temperature and the critical confinement length scale (e.g., thickness, pore diameter, etc.). In their work, Poniewierski and Sluckin [5] generalized Sheng's theory to ordered and disordered substrates and made a connection to the thermodynamic arguments of the Kelvin condensation, showing they are essentially the same phenomena.

In the decade following the above theoretical works, there have been a number of experimental efforts to observe the critical point in different confinement geometries and probing methods [6–9]. Of particular interest to this research is the work in classical wedge geometry by Yokoyama [10] who performed birefringence measurements in a wedge cell prepared with a spherical lens and a glass plate. His results showed good agreement with the Sheng-Poniewierski-Sluckin theory; however, he noted that the critical point has not been conclusively found due to finite resolution of the probing method. In 2001 Kočevar *et al.* [11] measured an emergent force when a glass bead mounted onto an AFM cantilever approached the silanized glass surface and was completely immersed in a nematic in the isotropic phase. The origin of the attractive force was attributed to the phenomenon of capillary condensation of the nematic order in a narrow gap between the flat surface and the bead. The transition temperature was found to rise with decreasing thickness of the gap and a critical point in the thickness-temperature phase diagram (d, T) was located, beyond which the transition became continuous. Later Stark *et al.* [12] considered capillary condensation between colloids in the isotropic phase of a nematic LC and constructed a phase diagram of the continuous and discontinuous formation of capillary bridges as a function of temperature and intercolloid distance at a fixed colloid radius. They found that for large enough colloids a critical point exists beyond which capillary bridge is formed smoothly. Further, they speculated that if two particles were brought close to an appropriate distance in the vicinity of the critical point small fluctuations in colloid positions would induce stochastic transitions between the bridge and no-bridge configurations. As it will become clear this last point especially may be important in explaining the observations we present in this work. We should also note that the experiments on nematic order condensation in thin layers of nematics were largely focused on static properties, such as optical retardation, and few

---

[*] Contact author: jaka.pisljar@ijs.si

experiments focused on dynamic properties using dynamic light scattering [13].

Much interest in recent years has been on the topic of skyrmions, the intriguing topological structures formed in diverse physical systems that possess a degree of chirality, such as thin magnetic films, Bose-Einstein condensates, and nematic liquid crystals. Skyrmions are topologically protected structures of continuous fields that cannot be unwound into a homogeneous background with any combination of smooth deformations, such as rotations or translations [14]. This fact is reflected in their relative robustness and offers magnetic skyrmions as candidates for key components of future memory storage devices [15]. As topological objects, skyrmions are also assigned a topological charge Q, which counts the number of times a continuous field vector (e.g., magnetization, director, etc.) of a skyrmion wraps around a unit sphere, onto which the field vector is mapped. In the strictest definition $Q \geqslant 1$ is an integer, but in addition to the most widely described full-skyrmions, with $Q = 1$, fractional skyrmions with $Q < 1$, can also be stabilized and were recently observed [16,17]. Three of the most intriguing LC phases, the blue phases (BPs), were long understood to comprise of double-twist cylinders that stack into body-centered cubic, simple cubic, and disordered structures for BPI, BPII, and BPIII respectively. An alternative view of these phases is that the constituent cylinders are actually quarter-skyrmionic filaments with $Q \sim 1/4$, as the director turns for $\sim 45^\circ$ in each double-twist cylinder. Unlike full skyrmions in a homogeneous background, these quarter-skyrmions are stabilized only by neighboring quarter-skyrmions and the surrounding disclination network. In our recent work [18] we demonstrated that when confined between two glass plates to thicknesses below the material's pitch, both BPI and BPIII transition into dense half-skyrmion (HS) lattices with a 90° radial twist.

As a continuation and extension of our previously published work [19] we present here additional illuminating experiments performed in ultra-thin layers of both achiral and chiral liquid crystals. For a sample of an achiral nematic wedged between two bare glass plates, we used high-resolution optical microscopy to observe and record a change in the nature of the phase transition from discontinuous to gradual with increasing confinement in the range of thickness from 20 nm to 500 nm. At confinements slightly above the thickness of gradual transition (i.e., around 80 nm) we observe characteristic flickering of nematic domains that continuously appear and disappear from the isotropic melt. A typical frequency of this flickering is unusually slow, i.e., ∼10–100 Hz, and much slower than order parameter fluctuations observed by DLS in submicrometer thin nematic layers [13]. In chiral samples of low chirality, the transition behavior remains very similar; however, for the strongly chiral samples the situation becomes in some ways quite different. In contrast to featureless fluctuating domains in achiral nematic, highly chiral liquid crystal exhibits thermally driven flickering of HSs in the regions where fluctuations are observed.

The paper is divided into two main parts. In the first part, we report on the experiments, including the analysis of the dynamic measurements alternative to the one published in [19]. In the second part, we extend the model previously used to describe the phenomena occurring in confined LC systems to explain the observed structural fluctuations.

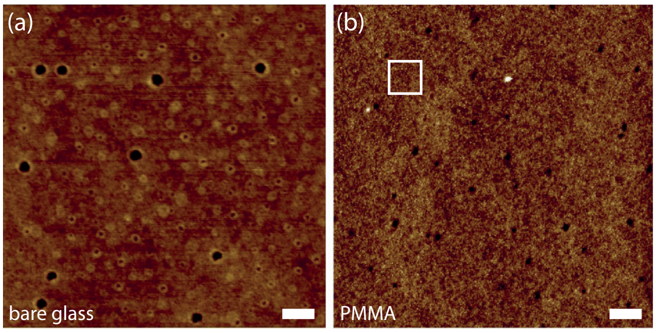

FIG. 1. AFM images of a bare glass surface and a glass surface covered with a thin layer of PMMA. Larger dark holes in (a) represent surface protrusions that are ∼6 nm deep and ∼30 nm wide, while their density is ∼50× higher compared to (b). These imperfections are likely related to the process of production of glass. Scale bars represent 100 nm and 1 μm in (a) and (b) respectively. White square in (b) represents the area of a region 1×1 μm^2, equal to the entire area shown in (a). Images taken by Miha Škarabot.

II. MATERIALS AND METHODS

In all of the presented experiments the LC samples were confined between two 150-μm-thick 25×25 mm^2 cover glasses (cat. no. 48366-089, VWR, Avantor, Inc.). For experiments with bare glass, the glasses were cleaned by rinsing with ethanol or isopropyl alcohol followed by mechanical wiping using Kimwipes and dried with pressured nitrogen. For experiments performed with poly(methyl methacrylate) (PMMA) -treated substrates, cover glasses were cleaned using the same procedure and treated with plasma directly prior to spincoating to enhance the adhesion of PMMA on the glass. A 1% solution of PMMA ($M_w = 900000$ g/mol) dissolved in methyl lactate was spin coated at 4000 rpm on each glass for 60 s and moved immediately on a hot plate at 170 °C for 3 min for baking. This produced a ∼25–30-nm-thick layer of PMMA, as confirmed by an atomic force microscope image of a cut made into the PMMA layer. Figure 1 shows AFM image comparison of both substrate types, bare glass and PMMA-covered surfaces, and reveals ∼50× higher number density of holes or dips in case of bare glass. In the case of either substrate, wedge samples were prepared by dropping a small 0.1–0.3 μl droplet of the observed material on one of the cleaned glasses placed on the hot plate heated to 40 °C and immediately covering it with the other glass. The droplet then spread quickly into a very thin layer which was left to equilibrate for at least 30 min on the hot plate with the sample in the isotropic phase.

Sample thickness was measured either before or after performing the phase transition observations by measuring spectra of broadband incandescent light reflected from the sample. Reference spectrum of light reflected from a chromium mirror is shown in Fig. 2(a). All spectral measurements were obtained with maximally closed aperture and field-of-view (FOV) diaphragms to ensure lowest achievable angle of incidence and measuring area respectively.

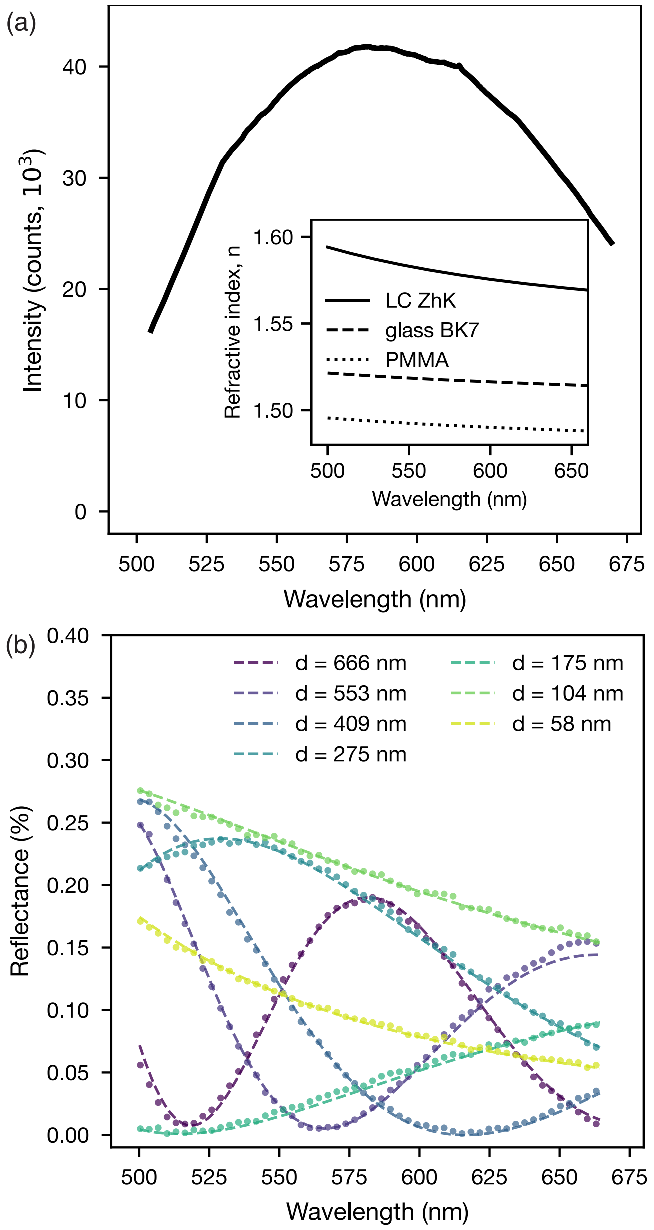

FIG. 2. Ultrathin cell thickness measurements. (a) Visible light range spectrum of incandescent light bulb used as a reference in thickness measurements. Inset: Chromatic dispersions of refractive indices of the LC (isotropic phase), glass, and PMMA layer. (b) Examples of measured reflection spectra (dots) and their fits (dashed lines) used to determine different thickness values.

During spectrum measurements, the sample was heated to the isotropic phase and the reflection spectrum was recorded at different positions. Reflection spectra were then fit using a thin film interference model, which included up to three distinct layers with known or approximated refractive index dispersions, shown in the inset of Fig. 2(a). The measured and normalized reflection spectra and their fits for a few different thicknesses are shown in Fig. 2(b).

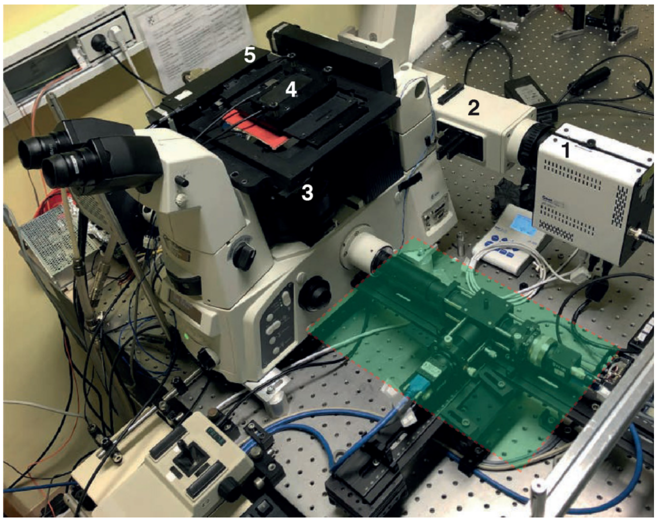

FIG. 3. Photograph of the microscopy system used for the described experiments. (1) Illumination LED source, (2) EPI illumination arm, (3) dichroic turret equipped with a 50:50 plate beamsplitter reflecting the light toward the sample, (4) heater and sample holder, (5) *xy*-translation stage for the sample. The setup in the green shaded region is used for cross-DDM measurements, which were not performed in this work; instead images and movies were taken with a single camera.

For achiral measurements on bare glass surfaces 4-cyano-4′-pentylbiphenyl (5CB) material (Fluorochem) was used. Chiral mixtures used in this work were prepared by combining the base nematic mixture material ZhK-1289 (Niopik, Moscow) [20] with chiral dopants CB15 and S811 (both Merck, KGAa). Mixing the ZhK-1289 with the right-handed chiral dopant CB15 in a weight ratio 1:0.65 produced a blue phase mixture with a cholesteric pitch of $p \sim 360\,\mathrm{nm}$ with a clearing temperature $T_{\mathrm{IN}} \sim 29\,^{\circ}\mathrm{C}$. To produce the longer pitch, non-BP forming, mixtures with similar temperature existence range, the base ZhK-1289 was first mixed with a right-handed chiral dopant CB15, lowering the transition temperature to a temperature range suitable for observations using oil-immersion objective, which is typically limited to temperatures below ∼37 °C. To slightly lower the chirality again, without affecting the transition temperature significantly, a left-handed chiral dopant S811 was added. The prepared mixtures contain these three components in a weight ratio (ZhK:CB15:S811) 1:0.5:0.1 for the $p \sim 710\,\mathrm{nm}$ mixture ($T_{\mathrm{IN}} \sim 31\,^{\circ}\mathrm{C}$) and 1:0.39:0.13 in case of the $p \sim 1200\,\mathrm{nm}$ mixture ($T_{\mathrm{IN}} \sim 34\,^{\circ}\mathrm{C}$). We denote the three chiral mixtures prepared using ZhK-1289 as nematogen as ZhK360, ZhK710, and ZhK1200 in order of decreasing chirality.

High-resolution optical observations were performed on an inverted Nikon Ti2 microscope with a motorized *z*-stage. The prepared sample cell was placed on a black background (black foil) of a custom built sample heater, designed for reflection microscopy, no. (4) in Fig. 3. Oil immersion objective CFI Plan Apo 100× oil with a very high numerical aperture of 1.45 was used to illuminate the sample as well as to collect light reflected from it. Considerable care was taken to minimize unwanted reflections. In addition to using oil immersion with a refractive index of $n_{\mathrm{oil}} = 1.518$ which closely matched that of the glass [see Fig. 2(a)], the sample was placed on a drop of immersion oil to maintain contact with a black foil. This setup ensured that any transmitted light

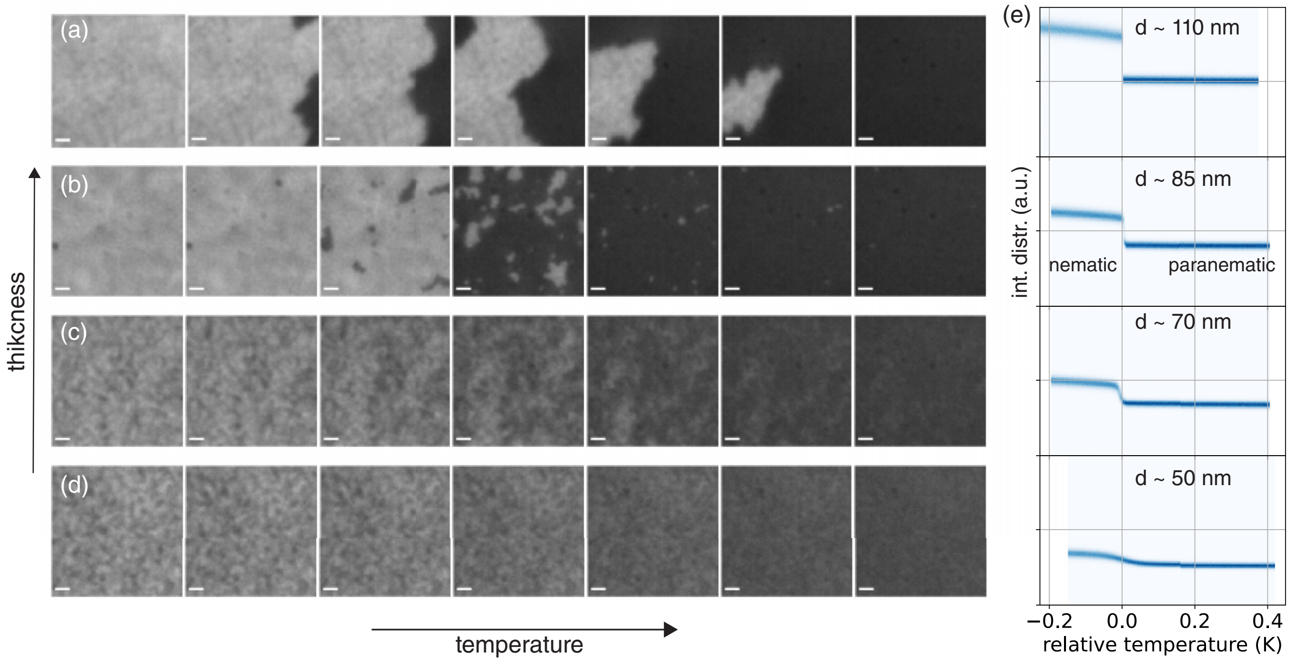

FIG. 4. Phase transition between a nematic and paranematic phases in an achiral nematic 5CB confined between two bare glass plates. (a)–(d) Images at different temperatures across the phase transition at different thicknesses. Scale bar represents 500 nm. (e) Intensity distribution (image histograms) as a function of temperature at different thickness values from thick at the top and thin at the bottom. They clearly show how an initially sharp transition at $T_{\text{rel}} = 0$ K widens with decreasing thickness. Note that the temperatures were shifted to relative temperature T_r.

was ultimately absorbed by the foil, ensuring that the majority of the reflected light came from the sample itself. The latter is due to a relatively higher refractive index mismatch between the glass ($n_g = 1.52$) and the sample ($n_o \sim 1.55$, $n_e \sim 1.76$ for 5CB at room temperature for $\lambda = 450$ nm [21]). While the samples were in the isotropic phase, the mismatch is due to the average refractive index $\bar{n} = (n_e + 2n_o)/3$. Once the director field $\mathbf{n}$ starts to order, the index mismatch becomes dependent on director $\mathbf{n}(\mathbf{r})$ orientation close to the glass surface plane Σ_g. Namely, if $\mathbf{n} \perp \Sigma_g$ index mismatch $\Delta n = |n_o - n_g| \sim 0.05$ for the plane polarized light, while when director lies in-plane $\mathbf{n}||\Sigma_g$ the index mismatch determining image brightness is $\Delta n = |n_e - n_g| \sim 0.15$, i.e., a few times larger. We used unpolarized blue ($\lambda = 450$ nm) LED light source CoolLed pE-300; see no. (1) in Fig. 3. If we assume the electric field at the sample mostly oscillates in planes parallel to Σ_g, the above mechanism holds and is useful to explain the origin of contrast in our images. With the use of short-wavelength illumination in combination with the high-NA objective we were able to achieve optical resolution better than ~150 nm.

Temperature stability and precise control were of high importance, due to the temperature fragility of the observed phenomena. Temperature was controlled by the above mentioned custom reflection microscopy heater which was in good thermal contact with the sample. To further stabilize the temperature the microscope objective was also heated to an elevated temperature of 25 °C, while room temperature was kept between 22 °C and 23 °C. Measurements of temperature using a pT-100 sensor positioned next to the sample when it is mounted on the microscope and shielded from air flow, showed temperature fluctuations below 5 mK. Imaging was performed using a Flir CM3-U3-50S5M CMOS camera, with 3.45 μm pixel size and 5 megapixel resolution. Usually an additional 2.5× magnification adapter was used in front of the camera making the magnification of the system 250× and pixel size on the captured images ~13.8 nm. Typical frame size was 400×400 pixels, covering a 5.5×5.5 μm^2 area of the sample. The camera with the magnification lens was mounted directly to the side-port of the microscope shown in Fig. 3 in place of the green shaded region.

III. EXPERIMENTAL RESULTS

A. N-I transition in achiral nematic

To observe the nature of the nematic-paranematic phase transition for a confined achiral sample, we performed measurements on a sample of pure achiral 5CB confined between two cleaned bare glass plates. As the sample was heated at a rate of 50 mK/ min across the phase transition temperature ~308 K, a series of images was taken in regular time intervals. This was repeated at several positions on the wedge sample with a known (measured) thickness profile, from thicker ($d \sim 500$ nm) to thinner ($d \sim 50$ nm) regions. Results are summarized in Fig. 4 and the dynamic behavior can be best observed in a video comparison found in Supplemental Video 1 [22]. In thicker layers, $d \gtrsim 100$ nm [see Fig. 4(a)] the transition appears distinctly first order: upon heating, the nematic phase disappears by rapid melting of the entire nematic domain visible in the FOV, with a sharp boundary between the nematic and isotropic phase. The coexistence temperature range observed within the FOV at this heating rate is $\lesssim$1 mK.

As we move to thinner regions, below the fluctuating transition thickness $d_f \sim 90\,\text{nm}$ [see Fig. 4(b)], the transition starts to appear dramatically different: the nematic phase does not melt as a larger domain but forms a distribution of nematic islands which melt and disappear, at slightly different temperatures. The coexistence range at the same heating rate is widened noticeably, with the phase transition taking place in 10–50 mK range. If we interrupt the heating within the coexistence region, e.g., at the temperature corresponding to the central image in Fig. 4(b), we can observe domain flickering of small nematic domains in different parts of the sample, close to the still formed nematic regions; see Supplemental Video 1, middle [22]. The system flickers between the bright nematic and dark isotropic phase and the switching appears to occur at random times and at a timescale of 10 ms. As we heat further, the flickering is observed in other regions of the FOV. As we move to even thinner regions, the coexistence temperature range continues to widen, while the size of melting domains reduces, as does the contrast between the paranematic and nematic phases in the images. This can be recognized well in Figs. 4(c) and 4(d); also see Supplemental Video 1, left [22]. These are clear indications we have crossed the critical thickness value d_c, below which the phase transition appears gradual. Beyond this point, experimental images and videos do not indicate melting but rather its *fading* into the paranematic phase; see Fig. 4(d). We discuss here phase transition appearance on heating; however, observe that a very similar behavior occurs upon cooling, as shown in Supplemental Video 2 [22] at a thickness of $\sim$85 nm.

In Fig. 4(e) we present stacked image intensity histograms as a function of temperature for different thicknesses [Figs. 4(a)–4(d)], which confirm the above description. All temperature scales are shifted to the same zero value by introducing the relative temperature $T_r = T - T_c(d)$, where in case of the gradual evolution of the OP T_c refers to the temperature, where the image intensity exhibits the maximal change. Note, however, that a several K temperature shift below $T_{\rm IN}$ was observed for $d \sim 50\,\text{nm}$. These graphs again show the change from the discontinuous (for $d \gtrsim 90\,\text{nm}$) to gradual phase transition behavior (for $d \lesssim d_c \sim 70\,\text{nm}$).

Let us focus on the region at thicknesses in the range $d_c < d < d_f$ where we observe the most intriguing phenomenon—the structural fluctuations. With bare glass plates used as confining surfaces, the fluctuations are very local: the domains appear and disappear at constant positions within a certain temperature interval. Typically a nematic structure appears at a particular temperature, flickers for a few mK below it and remains in the nematic phase at lower temperatures. The fluctuating features are of differing shapes from round to irregular and have lateral sizes from the resolution limit of $\sim$150 nm up to 1 µm. An example of a time sequence can be observed in Fig. 5, where two sequences of 4 consecutive frames are shown at a thickness of $\sim$85 nm. Images were taken at 25 fps, so the individual frames are 40 ms apart. To highlight the fluctuating features, we subtracted consecutive frames (shown with colors in the bottom rows) and plotted the resulting difference frames. In these images, the negative values correspond to features that had disappeared and are shown in blue, regions of no change (difference $\sim$0) are colored green and features that had formed in the time between two frames, corresponding to positive values in the difference frame, are colored yellow. In the bottom of Fig. 5 four frames acquired at more than 1 s later are shown. Image differences of these frames show that fluctuations appear in similar regions, some are marked with white and orange circles drawn with a full line. Concurrently in other regions, such as the one marked with a dashed circle, there is still no sign of fluctuating behavior. This persisting locality and heterogeneity within the frame is an additional hint, that the behavior is related to confinement and that the surface and consequently, the surface energy might play a key role in determining the local phase transition temperature.

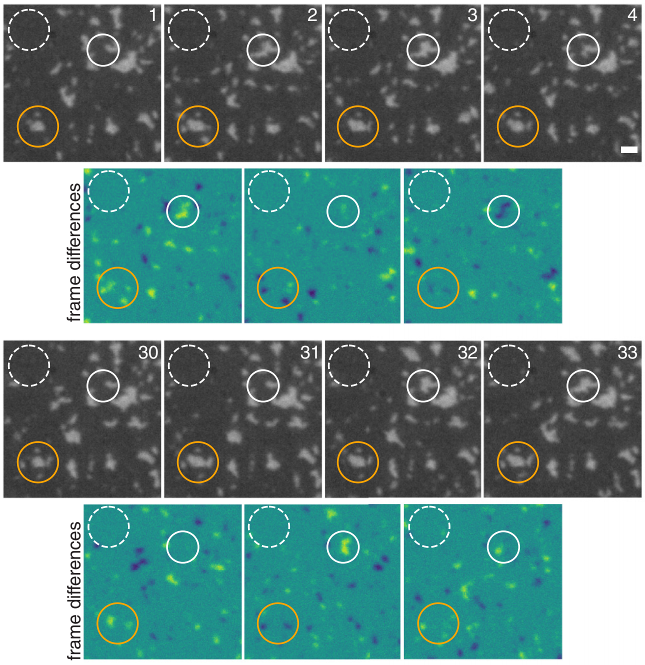

FIG. 5. Fluctuations in 5CB confined between two bare glass substrates. A sequence of four consecutive frames taken at 25 frames per second reveals multiple features appear and disappear during the duration between two frames. They can be easily observed when difference between two frames is calculated, yellow features appeared while blue disappeared between the two frames. Scale bar represents 500 nm.

We observed that phase transition temperature was shifted toward lower temperatures when the sample was confined between bare glass plates as well as when using PMMA-treated surfaces. This, as was shown in [5,10], suggests these confining surfaces are disordering for the nematic. The surface disordering influence can be visually confirmed when we observe the achiral 5CB sample $\sim$5 K below the transition in the bulk nematic phase shown in Fig. 6 for both types of surfaces. Low magnification transmission microscope image of a 5CB sample wedged between two PMMA treated glass plates shown in Fig. 6(a) indicates that the size of orientational domains reduces with thickness changing from a few micron on the right to a few 100 nm on the left. The behavior is analogous in the bare glass case, for which we show high resolution images in Figs. 6(b)–6(d). In these images, areas of similar shade correspond to regions in which the nematic director $\mathbf{n}$

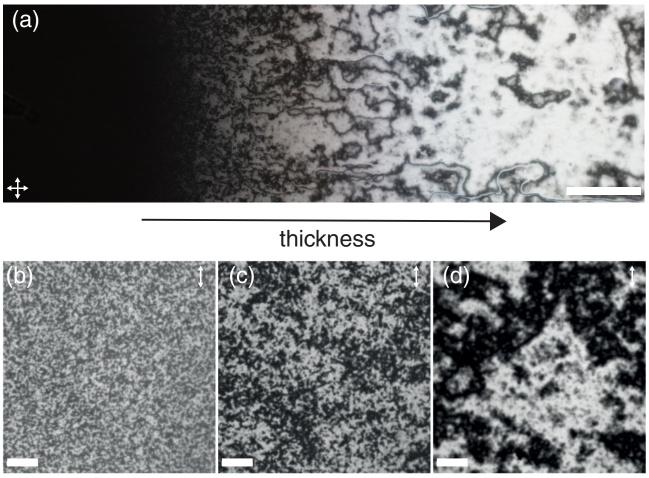

gradual transition

fluctuating transition

first-order transition

FIG. 6. 5CB wedged between two planar degenerate surfaces. (a) Low (10×) magnification image of 5CB confined between two spincoated PMMA surfaces inducing planar degenerate anchoring taken in cross-polarizer configuration. Wedge cell is formed with thinner part on the left-hand side and thicker (few micron) on the right. Scale bar represents 200 μm. (b)–(d) Images of 5CB between two bare glass surfaces taken using high magnification (100×, 1.45 NA) objective at regions where gradual, fluctuating and first-order phase transitions to the paranematic phase were observed. Images were taken in reflection using unpolarized light, but with inserted analyzer, direction marked with white arrows. Scale bars represent 500 nm.

points in a similar direction. The size of these orientational domains drops dramatically as we move to a strong confinement regime ($d \lesssim 100$ nm). At thicknesses significantly above this, where a clear first-order phase transition is observed, domains a few microns across are observed. As the surfaces are planar degenerate, such behavior is expected in very thick regions. This is because the domain orientation is determined by average directions imposed by the surfaces, even though their influence may be weak. As we near the region of fluctuating transition at $d \lesssim d_f$, the nematic structure starts to appear ruptured and domains reduce in size. Below this thickness the domains become less than 200 nm across. We may understand this behavior through considerations of energetic contributions: while in thick regions surfaces do influence the formed structure, the elasticity of the nematic is still able to drive the reorientation of neighboring domains, despite the cost energy of incompatibility at the surfaces. In thinner regions, however, the contribution of surface energy becomes relatively more significant due to the reduced overall volume. As a result, the formed domains more closely align with the locally imposed orientations of the two confining surfaces.

The discussion of dynamics in the achiral case was limited to the case of bare glass substrates. The use of an additional PMMA layer on the glass does not qualitatively change the phase transition appearance at different thicknesses, however it may cause the dynamics in the fluctuating region to appear different. Spincoating PMMA on the bare glass surface fills and smooths out the ∼10–50-nm-sized holes found on the bare glass (see Fig. 1) as well as provides a smoother surface in general [23,24]. This in turn causes the dynamics of these fluctuations to appear less constrained to certain positions in the sample, and this becomes more apparent in case of fluctuations in chiral mixtures, as we show below.

B. Transition in chiral mixtures

We also investigated the effect of confinement on mixtures with varying chirality strength in chiral nematics, which exhibit stable and observable HS when confined. The shortest pitch (highest chirality) mixture we used, was ZhK360 for which the first observation of liquid crystalline HSs [25] was reported for confinement thicknesses $d \lesssim 260$ nm and has a cholesteric pitch of $p \sim 360$ nm (see Sec. II). This mixture is appropriate, as it exhibits a stable BPI phase with an unusually large lattice distance (and consequently HS size) at temperatures not high above the room temperature. This allows for observations using an oil immersion objective, which is consistently kept in contact with the sample. We also used two additional mixtures with lower chirality, prepared using the same base nematic material ZhK-1289, with different concentrations of chiral dopants yielding longer pitch values of $p \sim 710$ nm and $p \sim 1200$ nm. A combination of left- and right-handed chiral dopants (see Sec. II) was used to bring the phase temperature to an appropriate range while realizing the desired pitch. These two mixtures do not exhibit BPs in bulk or in confinement; however, HS structures are still formed in thin layers, as shown in Fig. 7(b). For all three samples the equilibrium structure in thinnest regions a few degrees below the transition was planar unwound cholesteric, visually reminiscent of thin layer nematic structure, reflecting the planar degenerate anchoring of the confining substrates; see Fig. 7(a). Photographs of structures shown in Fig. 7 were taken at a few K below the respective bulk phase transition temperatures to the cholesteric phase. In certain thicker regions of these bare glass samples a uniform-lying helix structure was found and is shown in Fig. 7(c). The insets in these images show a line intensity profile along the marked yellow line and indicate the cholesteric pitch values of the mixtures.

Similar to the achiral case described in Sec. III A, the chiral mixtures also exhibit three distinct pathways of the first-order phase transition depending on the confinement strength. With decreasing thickness, we observe a transition that exhibits three distinct behaviors: it (i) is clearly discontinuous in the thicker regions, (ii) shows fluctuations in the intermediate region, and (iii) becomes gradual in the thinnest region. In the case of all three chiral mixtures roughly below $d \lesssim 100$ nm switching between the unwound cholesteric and paranematic phase is observed; see Supplemental Video 3 [22] for their visual comparison. As an example, Fig. 8 shows a sequence of five consecutive frames and their differences in the $p \sim 710$ nm mixture. Similarly to the case of the achiral mixture, there are regions within the frame where fluctuations are stronger and regions where they are weaker or nonexistent, indicating the importance of the local surface influence.

In the context of this work, the main difference between the three chiral mixtures is that the longer pitch mixtures exhibit the formation of HS only at thicknesses above which the fluctuating phase transition appears, that is above 100 nm.

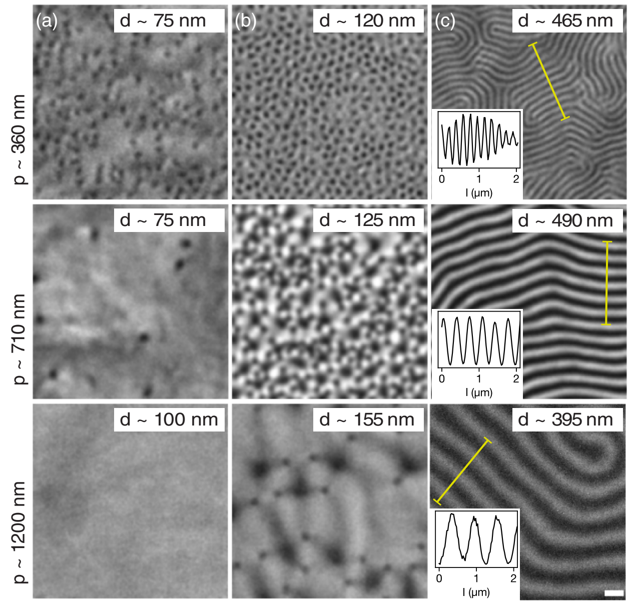

FIG. 7. Photographs of low-temperature structures observed at different confinement thicknesses d for three distinct pitch p values of ZhK-1289 mixtures used in our measurements. (a), (b) For all pitch values HS structures are observed as black dots, as less light is reflected from their center due to their director structure [18]. For longer pitch the accompanying $-1/2$ disclinations can be observed as well, they appear as smaller black dots. (c) At higher thicknesses the structure of uniform lying helix was observed. The insets for these photographs show the intensity graphs of the modulations along the yellow lines and indicate the scale of the cholesteric pitch. Scale bar represents 500 nm.

Additionally, while fluctuations in ZhK360 mixture are observed below $d_f \sim 90\,\mathrm{nm}$, they were observed below $d_f \sim 85\,\mathrm{nm}$ and $d_f \sim 75\,\mathrm{nm}$ in ZhK710 and ZhK1200 mixtures respectively, indicating the d_f value rises with increasing chirality (decreasing pitch). Note, that the exact values of d_f are challenging to determine, as the transitions into the fluctuating regions are not sharp. In the following, we focus on the shortest pitch mixture, in which the fluctuating region coincides with the thickness region where the density of HS is still relatively high which is of important consequence for the *shape* of the fluctuating features.

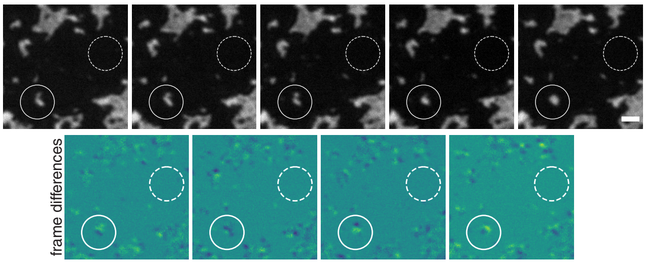

FIG. 8. Structural fluctuations observed in the chiral nematic of a $p \sim 710\,\mathrm{nm}$ pitch at confinement thickness $d \sim 80\,\mathrm{nm}$ between two PMMA-treated surfaces. Time difference between frames in the top row is 100 ms; bottom four images show differences between these sequential frames. Scalebar represents 200 nm.

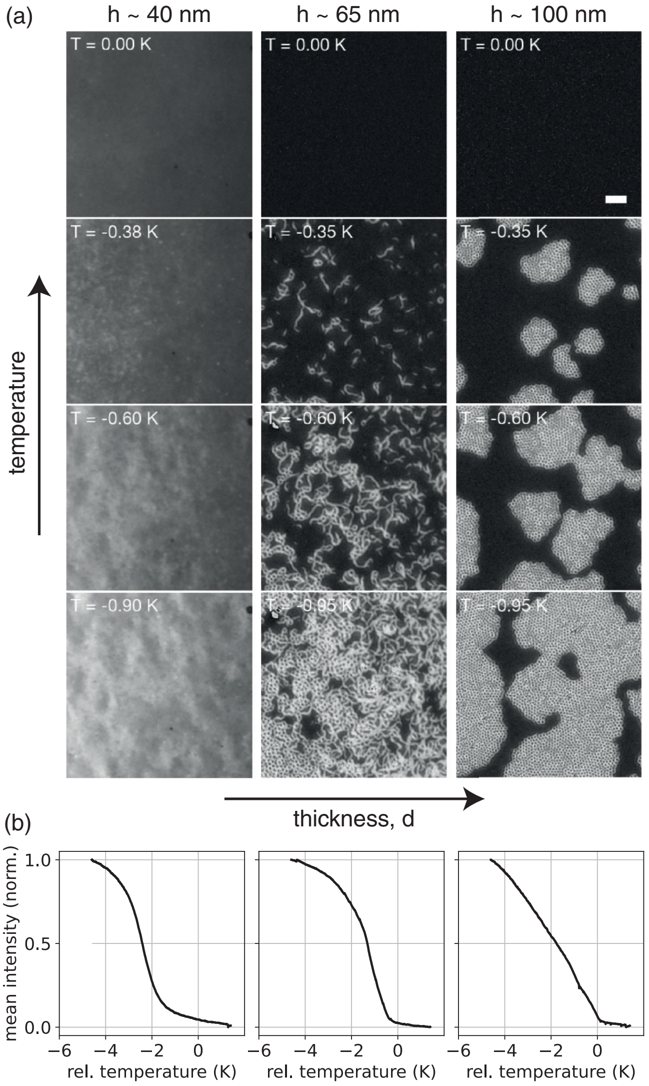

FIG. 9. Transitions from paranematic-HS phase in a ZhK-360 sample confined between two PMMA treated glass substrates. (a) The three columns at approximate thicknesses of 40, 65, and 90 nm (from left to right) show typical images taken at cooling from the paranematic phase of the sample between two PMMA treated glasses. Temperatures are relative to the paranematic phase in each case. (b) Mean image intensity of movies taken on cooling scans at three representative thicknesses. Temperature scales in all three cases are set relative to the transition in the thickest case.

To showcase the phase transition appearance change with thickness, we present images taken across the slow cooling ($-0.6\,\mathrm{K/min}$) transition of this mixture in Fig. 9(a) for three different thicknesses as sample is wedged between two PMMA-treated glass plates. The reader is also directed to [19] where the thickness-temperature phase diagram of this mixture is presented in Fig. 3. In Fig. 9(a) one immediately notices the relatively wide coexistence range of the paranematic phase and the structures in thicker regions. Compared to 5CB, which is a one-component LC, the base nematic ZhK-1289 for these three samples is a mixture of several nematogens [20] and when mixed with the chiral nematic CB15, exhibits a wider temperature coexistence range ($>1\,\mathrm{K}$)

of paranematic and cholesteric phases in thin as well as in thicker and bulk regions. Graphs in Fig. 9(b) show temperature dependencies of mean frame intensities for movie frames taken at cooling for these three phase transition regimes. Because the phase coexistence range is large, even in thicker regions, these graphs do not show as large jump in the mean intensity at the transition as was observed in the achiral case. In this case, it is the sharp up-turn in the rightmost column of Fig. 9(b) that signatures the onset of domain growth at the phase transition. It is to be compared with gradual up-turn in the leftmost column of Fig. 9(b), corresponding to the thinnest case, with the transition in the middle column of Fig. 9(b) somewhere between these two cases.

C. Dynamics of the paranematic-half-skyrmion transition

The most interesting dynamic behavior is observed at the transition shown in the central column of Fig. 9(a), where one can observe individual HS being actively created and destroyed at a 10–100 Hz rate, easily observable by the bare eye through the microscope, provided high enough optical resolution. Upon cooling from the paranematic phase, small, diffraction limited islands of the HS phase begin to appear at seemingly random positions, flickering at a fast rate. Occasionally an island appears and lingers for a longer time, growing larger and starting to form fluctuating elongated shapes that begin to curve. Such shapes sometimes close into isolated bright loops with dark centers within the paranematic background: these are HS existing as isolated entities in the paranematic phase. Supplemental Video 4 [22] shows a slowed down sequence of the described HS formation and its following decay. Upon further cooling much more such wormlike features start to appear, independently fluctuating and rearranging. The isolated HSs in the paranematic phase are observed only in the thinnest layers as in thicker parts HSs only form as dense more or less hexagonally arranged clusters.

Finally, as already mentioned above, the type of substrate also determines the appearance of these fluctuations. The above results were all obtained using PMMA substrates as use of bare glass substrates often restricted HS movement. We have often found the holes found in the bare glass acting as pinning sites for the individual HS. This can be appreciated in Supplemental Video 5 [22], which shows the difference in the dynamics appearance between the two substrates.

Real-space analysis of the dynamics

In Fig. 2 of [19] we presented the differential dynamic microscopy (DDM) characterization of the domain-HS flickering dynamics. To offer an alternative view, here, we present real space analysis based on a particle tracking algorithm [26] on these fluctuating structures in the same set of data. In a series of measurements we captured videos of these fluctuations at different temperatures when cooling slowly through the phase transition at a thickness of ∼85 nm. The videos consisting of 6400 frames were taken at a frame rate of 160 frames per second with 5 ms exposure time for a total duration of ∼40 s at each temperature. The frame rate was sufficient to follow the dynamics on frame-by-frame basis: see an example video of structural fluctuations of 1000 frames taken at $T_r = -0.2$ K in Supplemental Video 4 [22]. In the subsequent analysis we were mainly interested in the rate at which the structures appear and disappear and how this rate changes with temperature.

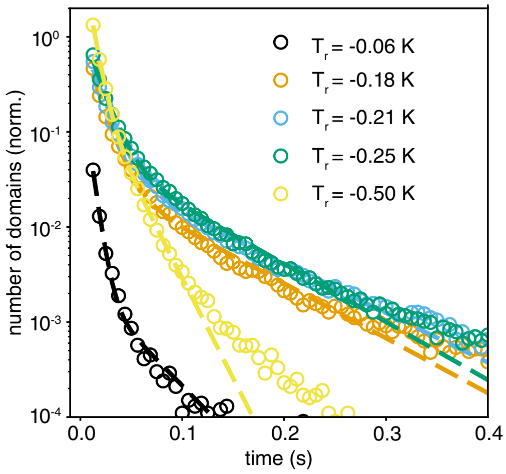

FIG. 10. Determined lifetime distributions of fluctuating HS and their parts at different relative temperatures obtained from dynamic analysis in case of ZhK360 confined between two PMMA covered glass substrates. The distributions are normalized to values close to 1, whereas typically, statistics of 10^4–10^6 domains was acquired. They were fit using a two exponential decay function; see Eq. (1).

The goal of the analysis was to directly extract the average time of existence (lifetime) of the structures at each temperature. A lifetime of a domain (also structure or feature) has an obvious interpretation at high temperatures, where features appear and disappear in different locations all over the frame of view. Domain lifetime equals to the number of consecutive video frames in which that particular domain is detected. To express it in time units, the number of frames is multiplied by the time between two frames. Definition is more challenging at lower temperatures, where a dense network of structures is gradually formed. After consideration, lifetime of a feature or structure was defined as the number of frames it can be observed to exist on its own: as soon as it is merged with another structure or a structure splits, the event enters the statistics as an end of life event for that structure. After such analysis was performed on all frames at a particular temperature and all detected structures, a large statistic of structure lifetimes was obtained. We then plotted a histogram distributions for the lifetime values as a function of real time, setting the time between the two frames to be the inverse of the acquisition rate. Examples of lifetime distributions is shown in Fig. 10. The distributions are drawn in log-linear scale and show signs of multistage decay processes, consisting of a fast and slow decay processes. The dashed lines are two exponential fits to the data of the following form:

$$f(t) = a_{\text{fast}} e^{-r_{\text{fast}} t} + a_{\text{slow}} e^{-r_{\text{slow}} t}, \qquad (1)$$

where a_{fast} (a_{slow}) and r_{fast} (r_{slow}) are amplitudes and relaxation rates of the fast (slow) modes respectively. Figures 11(a) and 11(b) then show the fast and slow relaxation rates and their relative amplitudes respectively, as obtained from these fits. In the column on the right side a temperature sequence

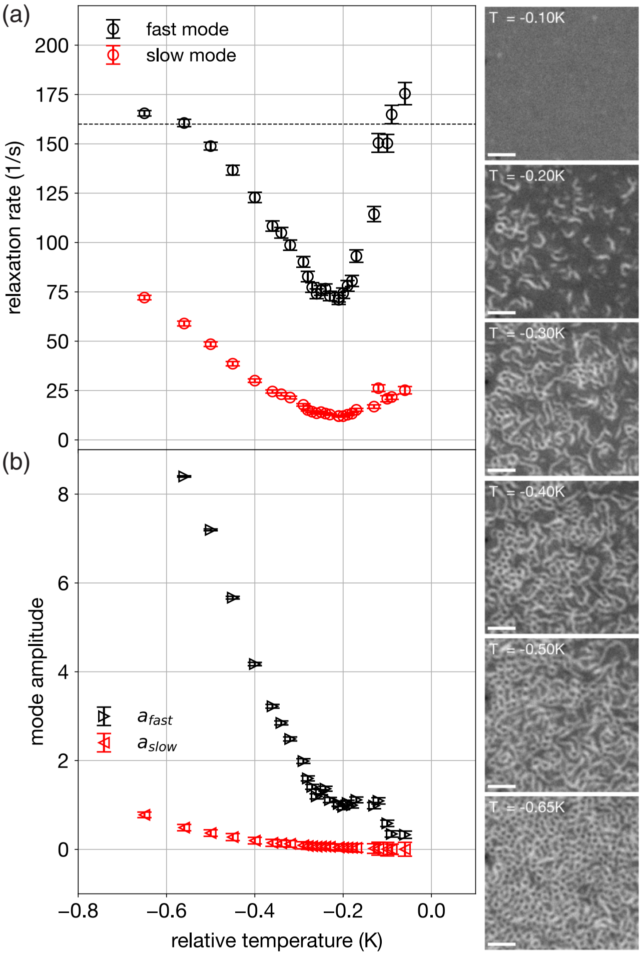

FIG. 11. Feature-tracking analysis of structural fluctuations in a sample of ZhK360 mixture confined between two PMMA-covered glass substrates. Relaxation rates (a) and amplitudes (b) of the fast and slow modes obtained from the fits to the lifetime distributions histograms, as the ones shown in Fig. 10. The dashed horizontal line in (a) marks the frame rate at whitch the analyzed videos have been obtained. Right column: Typical measurement frames at decreasing temperatures. Scale bar corresponds to 500 nm.

of representative frame cut-outs from these measurements are shown.

We see from Fig. 11(a) that the fluctuations appear to slow down, on average, as we cool from the paranematic phase at relative temperatures $T_r > 0$ K. The next noticeable feature is the minimum at $T_r \sim -0.2$ K, more apparent in the fast, but also visible in the slow relaxation rate. These minima occur at a temperature at which the mean distance between the fluctuating structures become comparable to their average size. Below this temperature, the relaxation rates begin increasing again. We explain this, by noting our definition of structure lifetime, described above. Until structures are well separated, i.e., roughly down to the temperature of the described minimum, events contributing to lifetime statistics are mostly formation and melting of the structures into the background paranematic phase. With decreasing temperatures the network of structures becomes more connected and the contribution of events such as formation or splitting of two domains becomes larger. Such events appear on a fast timescale with structures often merging and splitting in successive frames.

D. Other chiral mixtures

Chronologically, we first observed the transitional fluctuations in the sample of ZhK360. This mixture was chosen for its rare properties of forming a long-pitch, close-to-room-temperature blue phase, which is stable in a rather wide window of a few K. Most importantly, the material forms HS lattices in which their separation is large enough to be observed using an optical microscope. However, after reporting on similar fluctuations in a much simpler nematogen material, 5CB, a natural question arises as to why not simply make a chiral mixture using 5CB and check whether the behavior is universal. To address it we performed a small number of experiments on chiral mixtures of 5CB with added chiral dopant BDH1281 in 4.5% w.t., 5.0% w.t., and 5.5% w.t. concentrations. This resulted in ∼320 nm, ∼290 nm, and ∼260 nm pitch values respectively. The latter two mixtures exhibit a bulk blue phase, while the 320 nm mixture does not. All three exhibit HS in thinnest layers, which are most clearly observed in the 320 nm mixture. Confined between two PMMA-treated substrates this mixture transitioned directly to the cholesteric phase upon cooling below ∼35 °C. In the thinnest layers we observed transition behavior completely analogous to the one described in Sec. III B for the ZhK360 mixture. This can be observed in Supplemental Video 6 [22]. The temperature range of coexistence between the half-skyrmions and the isotropic phase is indeed narrower in the 5CB chiral mixture, ∼0.4 K, compared to $\gtrsim$1 K for the ZhK-1289 chiral mixture. Note that this range is still significantly wider compared to the (pure) achiral 5CB at comparable thicknesses, as the chiral sample is nevertheless a mixture of two materials with different transition temperatures individually. Furthermore, the video shows why selection of ZhK-1289 mixtures was better suited for dynamic analysis of these fluctuations. Specifically, the contrast of the structures on the isotropic background is significantly higher in this case, facilitating more accurate detection and tracking of the fluctuating domains and reducing potential sources of error. The contrast differences most likely stem from the difference in average refractive indices of the two mixtures, which influence the thin-film interference at the wavelength of observation. As a result, the 5CB mixtures exhibit higher background reflection at comparable thicknesses, reducing the visibility of the structures of interest.

IV. THEORETICAL MODEL

To identify dominant mechanisms governing the experimental observations we start with a full 3D Landau–de Gennes phenomenological model of our system, as introduced in Appendix A. We simplify the model using an uniaxial approximation (Appendix B) and focus on influence of the surfaces. In part this model was already presented in [19] and its supplemetal material.

A. Bulk and expected surface-driven effects

The bulk equilibrium phase behavior of the achiral LC described by Eqs. (A4)–(A6) is as follows [27]. The system exhibits the first-order isotropic-nematic transition at the bulk phase transition temperature $T_{IN} = T^* + b^2/(4a_0c)$. Above T_{IN} the order is melted, i.e., ($S = 0$), while below T_{IN} a spatially homogeneous orientational long-range order is established along the symmetry-breaking direction $\mathbf{n}$ with the amplitude

$$S_{eq} = S_0\left(\frac{3+\sqrt{9-8r}}{4}\right), \tag{2}$$

where

$$S_0 = S_{eq}(T_{IN}) = \frac{b}{2c}, \quad r = \frac{T-T^*}{T_{IN}-T^*}. \tag{3}$$

The subscript *eq* marks the global equilibrium value of S. S_0 is the value of the OP at the phase transition and r is the reduced temperature. The system exhibits bi-(meta)stable regime between the supercooling T^* and the superheating temperatures $T^{**} = T^* + \frac{9b^2}{32a_0c}$. When nematic LC is sandwiched in a plane-parallel cell, where both plates enforce identical isotropic tangential anchoring, diverse nematic structures could be stabilized depending on the cell thickness, temperature, LC material properties, and surface wetting interaction strength [4,28–34]. Among a rich palette of phenomena we focus on those relevant to our study. The interaction with surfaces might give rise to wetting phenomena and additional surface phase transitions. Theoretical and numerical studies based on Landau–de Gennes phenomenological model reveal that surface wetting interaction which promotes the nematic order and is linear in Q is the key generic mechanism for such effects [4,27,28,30,32]. Simulations show that there is an interval of wetting strengths W for which a first-order surface phase transition exist prior to bulk I-N transition on decreasing temperature [4,30]. The corresponding phase transition temperature monotonously increases with W. At a critical value of W the critical point is reached at which the discontinuous nematic layer formation is replaced with continuous growth of nematic order on decreasing T, until the bulk phase transition is reached. Therefore, in this case we have “localized” change in phase ordering behavior, in which only molecules in both surface layers are involved. Furthermore, disordering surface interactions tend to enforce surface dewetting transition below the bulk phase transition [35]. If the cell thickness is small enough (i.e., comparable to the nematic OP correlation length ξ) then the whole LC volume experiences effectively the surface interaction field. Therefore, in this case at the critical point the global phase behavior changes [4,30].

Note that these studies were made using mean-field approach neglecting fluctuations in the nematic order which tend to inhibit orientational order. Therefore, in thin enough cells (which are effectively two-dimensional) a Kosterlitz-Thouless [36] type order-disorder crossover on varying temperature might also be expected mediated by unbinding and binding of topological defects. However, there are several experimental reports [31–34,37,38] which support key mean-field-based predictions. For example, surface phase transitions near confining walls and transition qualitative change on varying the surface wetting interaction were detected [33] using optical birefringence and light scattering measurements. Furthermore, several experimental studies of nematic LCs confined to cylindrical [38] or other porous environments (e.g., controlled pore glass [37]) evidence existence of the critical point in the relevant phase space where the 1st order paranematic-nematic order is replaced by continuous evolution of nematic order. Generally, in these studies the critical point existed if the characteristic linear confinement size was comparable (to order in magnitude) to the nematic correlation length.

In the following we study response of a planar system close to the confinement-induced critical thickness d_c where the paranematic-nematic (P-N) transition ceases to be discontinuous. Here paranematic order refers to weakly ordered nematic order which appears due to confining surfaces ordering tendency [i.e., $w_1^{(1)} > 0$ in Eq. (A6)]. We determine (i) the P-N phase transition temperatures for selected material parameters and geometrical properties of the system in subcritical regime, and (ii) the critical condition at which P-N transition ceases to be discontinuous. We proceed by analyzing the hopping dynamics of LC domains between nematic and paranematic ordering in the temperature range, where LC exhibits bistable regime. We note that a single set of numerical parameters was used for all the numerical results which are reported below. They are listed in Appendix D and were selected so that the critical transition thickness was $d_c \sim 79$ nm and the negative transition temperature shift were close to what was observed experimentally.

B. Effective free energy density

We set that the nematic order is uniaxial and introduce simplifications in Appendix B. Furthermore, we neglect spatial variations in S, an assumption sensible in the vicinity of the critical point. We use the approximation of equal Frank nematic elastic constants [Appendix B, Eq. (B9)]. The resulting spatially averaged dimensionless effective free energy density $g = f/f_0$ reads

$$g(s) = r^{(\mathrm{eff})}s^2 - 2s^3 + s^4 - \sigma s, \tag{4}$$

where $s = S/S_0$ [see Eq. (3)] is the scaled OP amplitude, and $f_0 = a_0(T_{IN} - T^*)S_0^2$. Furthermore the effective dimensionless temperature $r^{(\mathrm{eff})}$ and the dimensionless effective ordering field σ are defined as

$$r^{(\mathrm{eff})} = \frac{T-T^*}{T_{IN}-T^*} + \frac{\xi_{IN}^2}{d^2}g_e + \frac{1}{d}\frac{2\xi_{IN}^2}{l_e^{(2)}} = r + \kappa, \tag{5}$$

$$\sigma = \frac{\xi_{IN}^2}{d^2}g_{24} + \frac{1}{d}\frac{2\xi_{IN}^2}{l_e^{(1)}}, \tag{6}$$

where we additionally introduced κ as the temperature shifting parameter. Parameter σ stands in the term linear in s and drives the disappearance of the discontinuous jump in the OP s. See Fig. 12(a) for the effect of varying σ at fixed κ, and Fig. 12(b) for the effect varying κ at constant σ. Dimensionless quantities g_e and g_{24}

$$g_e = \frac{1}{2d}\int[(\nabla\cdot\mathbf{n})^2 + (\mathbf{n}\cdot(\nabla\times\mathbf{n}) - q)^2 + |\nabla\times\mathbf{n}|^2]\mathrm{d}^3\mathbf{r}, \tag{7}$$

$$g_{24} = \frac{1}{d}\int \nabla\cdot[\mathbf{n}\nabla\cdot\mathbf{n} - (\nabla\mathbf{n})\mathbf{n}]\mathrm{d}^3\mathbf{r} \tag{8}$$

measure elastic distortions in the nematic director field. Note that only the values of g_e and g_{24} are distinct between the chiral and achiral LC cases. In bulk equilibrium nematic or

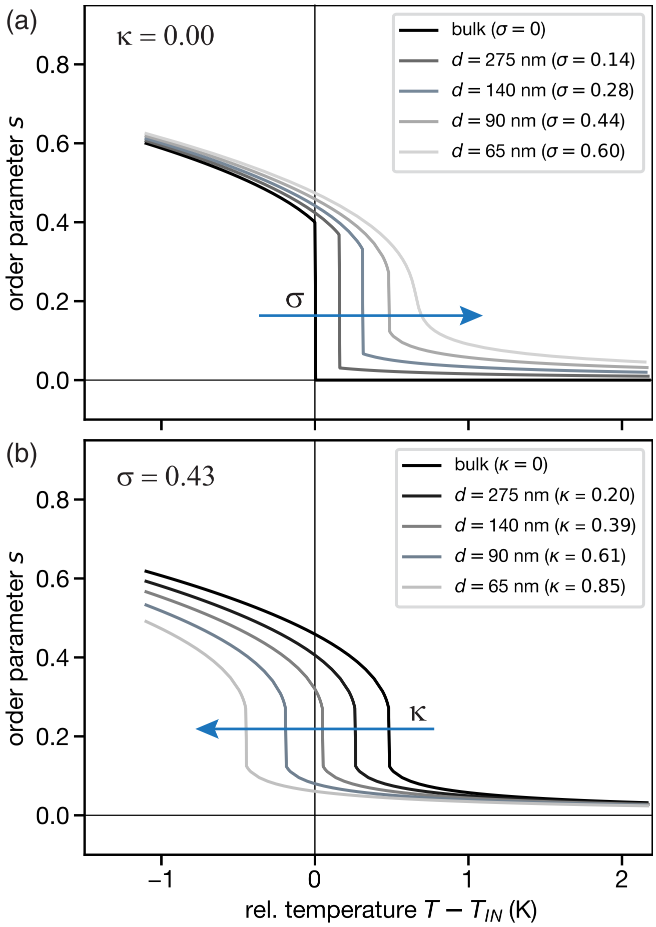

FIG. 12. Scaled OP s dependencies on temperature relative to its bulk transition value. (a) The dependencies were calculated at different thickness values, determining the value of σ, where value of κ was kept constant at $\kappa = 0$. Increasing σ changes the phase transition from discontinuous to gradual. (b) Here, $\sigma = 0.43$ was selected and kept constant, while value of κ was calculated from thickness. Varying κ only shifts the transition temperature and does not change its order.

cholesteric phase it holds $g_e = g_{24} = 0$. We expressed the quantities above in terms of thickness d and characteristic material dependent lengths [27]:

$$l_e^{(1)} = \frac{L_0 S_0}{w_1}, \quad l_e^{(2)} = \frac{L_0}{w_2},$$
$$\xi_{IN} = \sqrt{\frac{L_0}{[2a_0(T_{IN} - T^*)]}}. \tag{9}$$

Here $l_e^{(1)}$ and $l_e^{(2)}$ stand for the surface extrapolation lengths, related to the two anchoring values w_1 (ordering) and w_2 (disordering) respectively; see Appendix B, Eq. (B4) for their relation with constants used in Eq. (A6). Parameter ξ_{IN} is the bulk OP coherence length; see Appendix D for the list of all the numerical constant values used in this work. Values for quantities in Eqs. (9) were taken at the bulk transition temperature $T = T_{IN}$. Furthermore, we quantify dynamics of our system with respect to the bulk nematic OP relaxation time

$$\tau_{IN} = \frac{\gamma}{2a_0(T_{IN} - T^*)}, \tag{10}$$

expressed at $T = T_{IN}$ as well. The typical OP relaxation rate, i.e., $1/\tau_{IN}$ in an isotropic phase of a bulk nematic close to the transition temperature is ∼1 MHz.

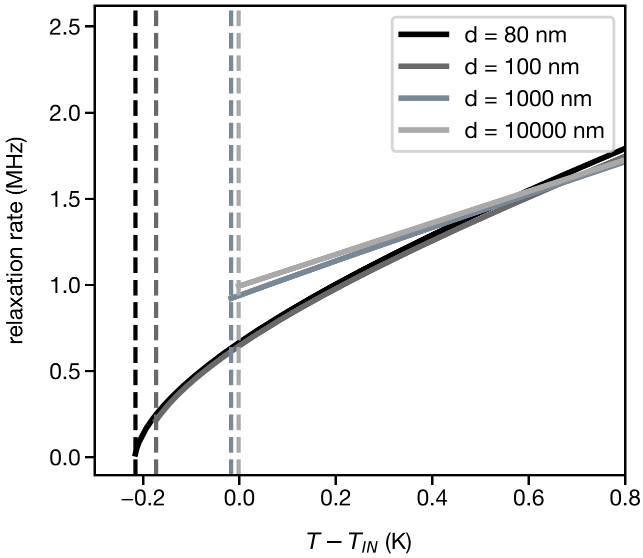

FIG. 13. Relaxation rate as a function of temperature at different confinement thicknesses.

C. OP relaxation dynamics

According to the Landau theory a critical slow down of OP relaxation dynamics is expected when a phase transition is approached. At the same time, the size of fluctuating domains ξ_i is expected to diverge at the phase transition. Both ξ_i and the relaxation time τ_i are related to the curvature of the corresponding phase free energy minimum and can be written as

$$\frac{\xi_i}{\xi_{IN}} = \frac{1}{\sqrt{g_i^{(2)}}}, \quad \frac{\tau_i}{\tau_{IN}} = \frac{1}{g_i^{(2)}}, \tag{11}$$

where we denoted $g_i = g(s_i)$ and $g_i^{(2)} = \frac{1}{2}\frac{\partial^2 g^{(\mathrm{eff})}}{\partial s^2}(s_i)$ represents the curvature of the corresponding minimum ($i = P, N$) in Fig. 15(a). Due to confinement related terms in the free energy through σ the minima of $g(s)$ are flattened at all temperatures which could explain the slower OP fluctuations in confined regions. Figure 13 shows the temperature dependence of the OP relaxation rate $1/\tau_P$ as the phase transition in approached from above, at different confinement thicknesses (different σ and κ). One can observe the substantial slowing down of the OP relaxation rates as the thickness approaches the numerical critical thickness $d_c \sim 79$ nm. One, however, immediately notices that while there is a considerable slow-down of the fluctuating rates, it is not quite what is observed experimentally. Furthermore if we plot the graph in the log-linear scale, we can see that the rates 10–100 Hz, observed experimentally, are numerically found only in an extremely narrow range of temperatures, namely just nK away from the transition.

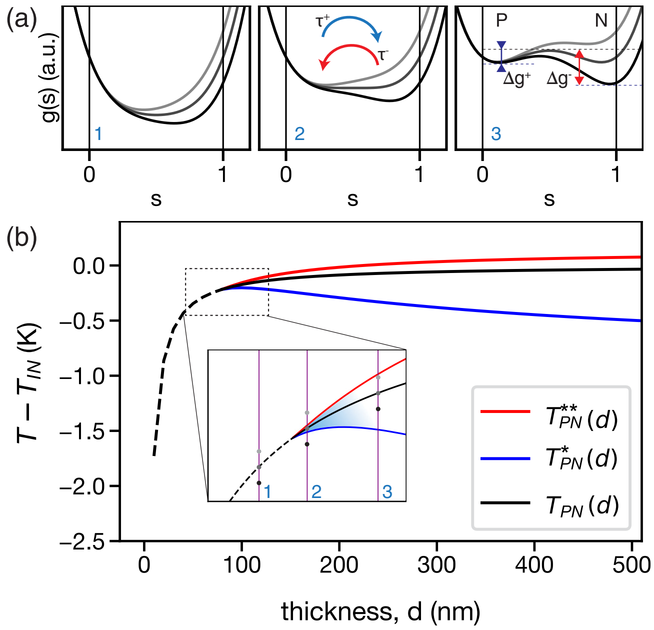

FIG. 14. (a) Condensation energy density $g(s)$ graphs at three different thicknesses (1–3) marked in the inset with small dots. of (b). The three curves shown in each graph correspond to three equidistant temperature values below, at, and above the $T_{PN}(d)$ value. (b) Calculated thickness dependencies of the supercooling $T^*_{PN}(d)$, superheating T^{**}_{PN}, and the transition temperatures $T_{PN}(d)$. The dashed line appears below the critical thickness, where the phase transition becomes gradual. Inset shows a zoomed-in region of the diagram, where occurrence of fluctuations is energetically viable.

D. Critical behavior

Phase behavior of the resulting system exhibits a critical point, which is determined by the condition [39]

$$\sigma = \sigma_c \equiv 0.5. \tag{12}$$

Further, if the saddle splay contribution is negligible then it holds

$$\sigma = \frac{d_c}{2d}, \tag{13}$$

where d_c stands for the critical thickness. In the regime $0 < \sigma < \sigma_c$ one obtains first order paranematic-nematic phase transition at the phase transition temperature $T_{PN}(d)$ determined by the condition [39]

$$r_c^{(\mathrm{eff})} = 1 + \sigma. \tag{14}$$

It follows that the thickness d dependent paranematic-nematic transition temperature $T_{PN}(d)$ can be written as

$$T_{PN}(d) = T_{IN} + (T_{IN} - T^*)\left[\frac{\xi_{IN}^2}{d^2}(g_{24} - g_e) + \frac{2\xi_{IN}^2}{d}\left(\frac{1}{l_e^{(1)}} - \frac{1}{l_e^{(2)}}\right)\right]. \tag{15}$$

This dependence is shown in Fig. 14(b) using a black line. It indicates the decrease of the transition temperature with reducing thickness as is expected for disordering surfaces in which $l_e^{(1)} > l_e^{(2)}$. The red (blue) line shows dependency of superheating (supercooling) temperature dependency, which corresponds to a temperatures at which the local minima of the paranematic (nematic) phases in $g(s)$ finally disappears and only a global $g(s)$ minimum remains. The intermediate range between these two temperatures gets narrower with decreasing thickness.

E. Hopping dynamics

We now offer a simplistic model with which it is possible to explain the observed dynamics. The model is based on the theoretical grounds established in the previous section and extended to phase hopping between the two competing phase minima s_i, corresponding to the isotropic, or in in thin layers paranematic, $i = P$ and nematic phases ($i = N$). The minima of $g(s)$ are schematically shown in Fig. 14(a). Transitioning between the two minima is only possible at temperatures where they exist, i.e., between the supercooling and superheating temperatures shown in Fig. 14(b). In this temperature region, the probability or conversely the hopping rate τ_h of such jumps can be estimated in the following form:

$$\tau_h^{(+)} = \tau_P e^{\beta \Delta E^+}, \quad \tau_h^{(-)} = \tau_N e^{\beta \Delta E^-}, \tag{16}$$

where $\beta = 1/k_B T$, τ_P, and τ_N are OP relaxation times of the paranematic and nematic phases respectively defined in Eq. (11). $\Delta E^{(+)}$ [$\Delta E^{(-)}$] are the heights of the (local) energetic barriers the system needs to overcome to transition from the paranematic (nematic) to nematic (paranematic) phase. Such considerations make sense when $\Delta E^{(\pm)}\beta \gtrsim 1$.

Let us consider a case when a cylindrical bridge of nematic (paranematic) phase with radius r_D is formed between two confining substrates at a thickness d, while the rest of the volume remains in the paranematic (nematic) phase. The change of nematic phase volume is $\Delta V_{PN} = d \times \pi r_D^2$. Condensation of such a nematic bridge is written as

$$\Delta E^{\pm} = E^{\pm}_{\mathrm{cond}} \pm E_{\mathrm{intrf}} \tag{17}$$

involving two energetic terms: (i) a term $E^{\pm}_{\mathrm{cond}}$ related to the condensation (+) or annihilation (−) of a new phase and (ii) a surface term E_{intrf} related to the cost of the creation/disappearance of an interphase boundary $\Delta A = 2\pi r_D \times d$. The first term can be written as

$$E^{\pm}_{\mathrm{cond}} = f_0 \Delta g^{\pm} \Delta V_i, \tag{18}$$

with

$$\Delta g^+ = g(s_m) - g(s_P), \quad \Delta g^- = g(s_m) - g(s_N), \tag{19}$$

which are denoted in Fig. 14(a) in the energy density schematic 3. The reduced OP s_i is the value in the two minima ($i = P, N$) or the maximum between them ($i = m$). The second term is written as

$$E^{\pm}_{\mathrm{intrf}} = \gamma_{PN} \Delta A_i = \gamma_{IN}(s_N - s_P)^2 \times \sqrt{g_i^{(2)}}\Delta A_i. \tag{20}$$

Here γ_{PN} is the paranematic-nematic surface energy, approximated by

$$\gamma_{PN} \sim \int (f - f(S_P))\mathrm{d}^2 r \sim \sim \int \frac{L_0}{2}|\nabla S|^2 \mathrm{d}^2 r \sim \frac{L_0 S_0^2}{2\xi_i}(s_N - s_P)^2, \tag{21}$$

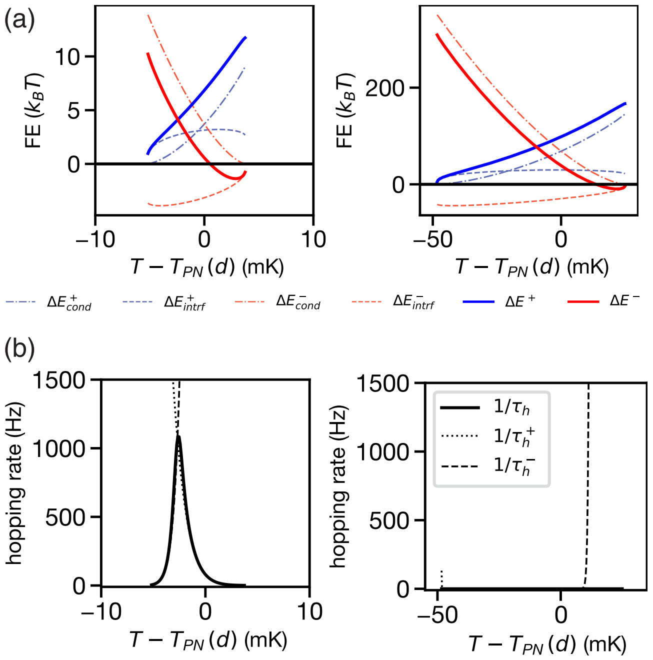

FIG. 15. (a) Energetic contributions to the cost/gain involved in a formation of a cylindrical domain with radius $r_D = 12\xi_{IN}$ at thickness $d = 85$ nm (left) and $d = 115$ nm (right). (b) Calculated individual and combined hopping rates in case of energy costs shown in (a).

where the integral runs over the domain interface width, roughly given by ξ_i, where $i = P, N$ for the paranematic and nematic phases. We also used a relation

$$\gamma_{IN} = \frac{L_0 S_0^2}{2\xi_{IN}} \tag{22}$$

for the bulk value of the nematic-isotropic surface tension, that is often measured experimentally [40,41]. The energy contributions $E^{\pm}_{\text{intrf}}$, $E^{\pm}_{\text{cond}}$ and their sum $E^{\pm}$ are shown in graphs of Fig. 15(a) at two different thickness values: at $d = 85$ nm, close to the critical thickness value with energies in the range of several k_BT and thus thermally accessible and at $d = 105$ nm where the energies required for hopping are high above the thermal energy values. The energy costs were calculated using the numerical parameters listed in Appendix C for a domain with radius size $r_D = 12\xi_{IN}$.

To proceed, we use the expression for the dimensionless free energy density $g(s)$, introduced in Eq. (4). This expression together with Eqs. 16 can be used to calculate the hopping rates $1/\tau_h^{\pm}$, shown in Fig. 15(b). We plot rates for hops in both directions and the combined rate for hopping $1/\tau_h$ which was determined as

$$\tau_h = \frac{\tau_h^+ + \tau_h^-}{(\tau_h^+)^2 + (\tau_h^-)^2}. \tag{23}$$

To calculate the rates we used energy costs presented in Fig. 15(a). Both $1/\tau_h^{\pm}$ and the combined rate τ_h, are shown in Fig. 15(b) for the two thickness cases considered. In the thicker case, where the $\Delta E \gg k_BT$, the hopping rates are 0 in majority of the temperature range, meaning such jumps are highly improbable. At temperatures close to both supercritical temperatures the corresponding rates quickly rise to high rates. This indicates the phase transition here occurs very rapidly, without fluctuations, like in the achiral case shown in Fig. 4(a). In the thinner case on the other hand there is a temperature region where probabilities for both jump directions are nonzero and approximately equal, resulting in the combined hopping rate of up to 1 kHz, for domains of size $r_D \sim 12\xi_{IN}$. Observation of such rates is predicted in several mK range vicinity of the local transition temperature, which is about 10–1000× less than what was observed in experiments and will be discussed in Sec. V.

F. Role of chirality

Finally, we consider the saddle-splay contribution to σ Eq. (12). Note that this term is equal to the Gaussian curvature K_G of the hypothetical surface determined by the surface normal pointing along $\mathbf{n}$ [27]. Consequently, we approximate the saddle-splay contribution by $g_{24}/d^2 \sim 1/R_{24}^2$. Here R_{24} approximates the characteristic linear radius of K_G. For $\xi_{IN} \sim 10$ nm one obtains the critical condition for $R_{24} \sim 14$ nm for $w_1 = 0$. One would expect that the characteristic distortion length typical would be given by combination of thickness d and the chiral pitch $p = 2\pi/q$, where q is the chirality. Therefore, we conclude that the surface interaction term plays dominant role in σ, although the saddle-splay contribution might also yield experimentally observable impact. Indeed, our measurements reveal that with increasing chirality (i.e., decreasing pitch) the critical thickness increases. The critical condition taking both contributions in Eq. (12) taking into account approximations described above yields

$$d_c = \frac{4\xi_{IN}^2}{l_e^{(1)}[1 - 2(\xi_{IN}/R_{24})]}. \tag{24}$$

One expects R_{24} to be comparable to p (note that $p > 0.1\,\mu\text{m} > \xi_{IN}$) and Eq. (24) reveals that the value of d_c increases with decreasing p.

V. DISCUSSION AND SUMMARY

We have described experiments based on high-resolution optical microscopy of near phase transition phenomena occurring in the sub-100 nm layers of (a)chiral nematics. Although predictions and experimental evidence of the critical confinement for LC systems have been known for decades, it has so far not been directly (optically) observed. After first observing the surprisingly strong and slow fluctuations in the ZhK360 mixture, our initial reasoning direction was that these are the slowed down classical fluctuations of the scalar OP which are in some way specific for this type of phase. OP fluctuations, in the sense of the Landau–de Gennes theory of the isotropic-nematic phase transition, are predicted to critically slow down when the system is cooled close to the critical temperature [42], and their size corresponds to the nematic coherence length ξ_{IN}. Such reasoning implied, that we are directly observing the condensation of the soft mode [43,44], which in the achiral case would be the nematic phase while in the sufficiently chiral case it would be the a form of HS structures. However, using simple theoretical considerations presented in Sec. IV and in [19] we have shown that the expected temperature range for existence of dynamics this slow and involving such large domains would be in the extremely narrow, nanokelvin, vicinity of the phase transition temperature. This is orders of magnitude below to what is actually observed, as shown in Fig. 4.

Analysis of our experimental data of fluctuations has shown, that we typically observe a wide range of relaxation times at each temperature and consequently also a wider transition region, both in achiral and chiral cases. Multiple arguments for such behavior exist. First, domains of different sizes are formed and this inevitably leads to distribution of relaxation and hopping times. Namely, in the uniaxial approximation the key quadratic free energy density terms determining the nematic amplitude within a domain characterized by the linear size ξ_D reads $f \sim a_0(T - T^*)S^2 + LS^2|\nabla \mathbf{n}|^2 \sim a_0(T - T_D^*)S^2$. Here we assumed [45] $|\nabla \mathbf{n}|^2 \sim 1/\xi_D^2$ and $T_D^* = T^* + \frac{L}{\xi_D^2}$. For example, in the isotropic bulk phase it holds $\tau \sim L/[a_0(T - T^*)]$. In confinement, determined by ξ_D, it follows $\tau \sim L/[a_0(T - T_D^*)]$ which depends on ξ_D. Therefore, distribution in ξ_D values enforces also distribution in OP relaxation time and domain hopping times τ_h. Domains of a range of sizes, including those much larger than the typical ξ_{IN} value, were observed to fluctuate at a single temperature and clearly fluctuations appeared very localized in different parts of the FOV, much more so in samples prepared by the achiral 5CB on the bare glass surface. In addition to the above, the predicted thickness range in which these fluctuations would be thermally accessible according to the classical Landau theory of the phase transition is again multiple orders of magnitude below what is observed experimentally. These hints directed us into additional consideration of the role of the surfaces. Although they play a crucial role in the change of the phase transition nature through wetting phenomena and capillary condensation below the critical confinement [3,5,10], it appears they also provide degree of inhomogeneity and randomness that facilitate a real-space landscape of energetic minima. Close to the critical confinement these minima become accessible through thermal fluctuations of the system near the transition temperature, as shown in Sec. IV E. In terms of the theoretical model this means our assumptions of uniform and constant anchoring strength and thickness were not completely justified. Indeed, allowing the anchoring parameters w_1 and w_2, which in turn determine σ and κ, to have (narrow) distributions around their mean values causes the fluctuation temperature range at certain thickness to widen. This could be caused by spatial variations of these two parameters, which is in line with experiments in which uniformity of LC-substrate interactions was probed [46,47]. Additionally, as revealed by the AFM images of the substrates presented in Fig. 1, the assumption of perfectly uniform thickness is not realistic, and the consequence of this is again transition width widening, as well as the observed distribution of relaxation rates across the field of view. In case of certain bare glass substrates of lower quality, which exhibited an even higher number density of holes, these acted as strong nucleation cores for the HS. At such hole sites the HS were condensed several tenths of K above the transition temperature for the rest of FOV.

The amorphous surfaces of glass and PMMA substrates effectively act as an external random field on the LCs during the phase transition, which connects our work to an abundance of research in this topic during the past 30 years. In case of static fields, the imposed disorder is typically referred to as quenched [47,48]. Imry and Ma [49] considered models of magnetic systems and postulated, that regardless how small the influence of random fields acting on a system with continuous symmetry of dimensionality below 4 is, compared to interconstituent interactions, the system will fall apart into domains of finite size. They predicted the expected domain size ξ_D as a function of the disordering field strength w as $\xi_D \propto w^{2/(4-D_{\mathrm{eff}})}$, where D_{eff} is systems effective dimensionality. In our case, markings of such behavior can be found in Fig. 6, which clearly shows domain growth with increasing thickness. A few years later Imry and Wortis [50] also discussed the influence of the quenched disorder induced by impurities on the first-order phase transition and predicted rounding of the discontinuity by increasing the concentration of random impurities in the system. They argued the transition rounding is due to fluctuations in the thermodynamic phase that start to appear due to local fluctuations of the impurity density. Additionally they discussed the possibility of spatial dimension of these fluctuations being much larger than the coherence length of the system.

Structural fluctuations appearing from the isotropic phase discussed in this work, correspond to spontaneous organization of $\sim 10^6$–10^7 nematic molecules in an orientationally ordered cluster, its sequential reshaping and eventual decay. All this happens on a timescale observable by a naked eye. This is reminiscent of phenomenon recently reported by Jeon *et al.* [51], where they observed reversible disorder-order transitions of Au nanocrystals formed by Au atoms obtained from a AuCN nanoribbon bombarded with electron beam of a TEM microscope, which was simultaneously used to image the sample. Movies of the Au nanocrystal nucleation process show that nucleation proceeds through a series of transitions between the disordered and crystalline states, forming and decaying on a timescale of ∼10 ms. Clusters of 10–100 Au atoms arrange into crystalline lattices with different orientations and decay back into the cluster of disordered Au atoms. This occurs many times before finally, after seconds of exposure to the electron beam, the expected crystal domain growth takes place. This is in contradiction with the classical nucleation theory [52] in which crystal nucleation is a single-step process with the domain atoms both clustered and ordered from the onset which requires the system to jump over a higher energy barrier. Although similar, the described structural fluctuations in our system do not fall under the usual description of nucleation and growth: one cannot speak of a clear critical cluster size, which would correspond to an individually formed nematic tactoid that remains stable and grows. In the temperature range of fluctuations, such growth is prevented by the surface influence, which effectively frustrates the formed domain forcing it to decay or reshape.

The dynamic analysis of the fluctuations in ZhK360, presented in Fig. 11, complements the DDM results presented in [19]. Indeed, both approaches to some extent confirm the observation that dynamics within a single FOV is highly nonuniform at each temperature, with certain parts of the FOV already in their steady equilibrium while others still exhibit strong fluctuations. However, the correlation functions obtained in the DDM analysis almost completely hide the fact of still observable dynamics below the relative temperature $-0.2\,\mathrm{K}$, due to the relatively higher static signal of the background long lived-structures. This is not the case in real-space analysis where fluctuating domains are clearly discriminated from the background and such events are detected. On the other hand, the cause for the increasing relaxation rate at temperatures $\lesssim -0.2\,\mathrm{K}$ must be understood separately from those above $\gtrsim -0.2\,\mathrm{K}$; see Fig. 11(a). On the lower temperature side the density of structures increases and with it, so does the number of domains existing on their own for a short time, as they soon merge or split from another. Increasing number of such events leads to seemingly higher relaxation rate in this temperature region. On the higher temperature side, the number of all events is relatively smaller as domains are well separated, and dynamics mostly consists of individual domains appearing and disappearing. The rate of these events indeed increases with rising temperature, in line with DDM results presented in [19].

In conclusion, we presented in this work a class of phenomena that was, to our knowledge, not previously observed albeit numerous experiments on strongly confined LC systems. Through direct optical observations using light microscopy we were able to capture the real-time structural fluctuations in achiral and chiral LC nematics in sub-100 nm layers. In achiral and weakly chiral samples the fluctuating domains are typically ∼100–500 nm islands of the uniformly oriented nematic while in the highly chiral samples they consist of active creation and annihilation of special chiral objects, HSs. In this work we characterized the dynamics of these HS fluctuations through real space analysis, using object tracking techniques, a complement to previously presented results. Additionally, we showed here that the observed HS fluctuations on transition are not unique to the materials we initially used to prepare them. Although more difficult to observe, they can be realized also using more easily accessible nematic materials such as 5CB. To understand the physics behind the observations and measured fluctuation rates, we proposed an extended phenomenological Landau–de Gennes model of confined (a)chiral nematic combined with the effect of disordering substrates. These impose a random and spatially inhomogeneous anchoring conditions on the sample, which influence the sample majorly in the thinnest layers and cause the energetic barrier between the ordered and disordered phase to reduce to a degree where thermal fluctuations can drive the stochastic phase transition jumps locally.

ACKNOWLEDGMENTS

This work was supported by the Slovenian Research and Innovation Agency (ARIS) through Contracts No. PR-08332 (J.P.) and No. P1-0099 (I.M.). A.N. and U.O. acknowledge support from NAS Ukraine (Grant No. 1.4.B/209). The authors would like to thank M. Škarabot for producing the AFM images. We thank the anonymous referees for their detailed and constructive feedback.

APPENDIX A: FULL THEORETICAL MODEL

Of our particular interest are nematic order fluctuations of a nematic LC confined within a plane-parallel cell of thickness d. As usual, we express the nematic orientational order at the mesoscopic level in terms of the traceless and symmetric tensor nematic order parameter (OP) [8,27]

$$\mathrm{Q} = \sum_{i=1}^{3} s_i \mathbf{e}_i \otimes \mathbf{e}_i. \tag{A1}$$

Here s_i are Q eigenvalues (the amplitude fields), and $\mathbf{e}_i$ the corresponding normalized eigenvectors. In the case of uniaxial order, where two eigenvalues are equal, $Q$is commonly represented as [27]

$$Q = S(\mathbf{n} \otimes \mathbf{n} - \mathrm{I}/3). \tag{A2}$$

The unit vector $\mathbf{n}$ is referred to as the nematic director (symmetry-breaking) field, S is the nematic OP amplitude field, and I stands for the unit tensor. Note that an uniaxial state can exhibit either positive or negative uniaxiality, corresponding to prolate or oblate mesoscopic OP geometric presentation. Next, we express the free energy F of the system as the sum of volume and surface contributions

$$F = \int (f_c + f_e)\mathrm{d}^3\mathbf{r} + \int f_s \mathrm{d}^2\mathbf{r}. \tag{A3}$$

The first and second integral are carried out over the LC volume and LC-confining substrate, and f_c, f_e, and f_s stand for condensation, elastic, and surface free energy density, respectively. We write them in their full form using the Cartesian coordinate system ($x_1 = x, x_2 = y, x_3 = z$) as [8,27,29,53]

$$f_c = \frac{3a_0}{2}(T - T^*)Q_{ij}Q_{ij} - \frac{9b}{2}Q_{ij}Q_{jk}Q_{ki} + \frac{9c}{4}(Q_{ij}Q_{ij})^2, \tag{A4}$$

$$\begin{aligned} f_e = {} & L_1^{(1)}Q_{ij,ij} + L_1^{(2)}Q_{ij,k}Q_{ij,k} + L_2^{(2)}Q_{ij,j}Q_{ik,k} \\ & + L_3^{(2)}Q_{ik,j}Q_{jk,i} + qL_4^{(2)}\epsilon_{ijk}Q_{il}Q_{jl,k} \\ & + L_5 Q_{ik,ij}Q_{jk} + L_6 Q_{jk}Q_{jk,ii}, \end{aligned} \tag{A5}$$

$$\begin{aligned} f_s = {} & w_1^{(1)}v_i Q_{ij} v_j + w_1^{(2)}Q_{ij}Q_{ij} + w_2^{(2)}(v_i Q_{ij} v_j)^2 \\ & + w_3^{(2)}Q_{ij}v_j Q_{il}v_l. \end{aligned} \tag{A6}$$

The indices i, j, k, l stand for any of the three orthogonal axes and sums over repeated indices are assumed. $Q_{ij,k}$ describes the partial derivative of Q_{ij} with respect to the kth coordinate, and ϵ_{ijk} is the Levi-Civita antisymmetric tensor. Numerical coefficients in Eq. (A4) are introduced for later convenience. Quantities a_0, b, c are Landau expansion coefficients, T^* is the bulk isotropic supercooling temperature, $L_i^{(j)}$ are generalized elastic constants, q describes the inherent LC chirality, $w_i^{(j)}$ are surface interaction constants, and $\mathbf{v}$ describes the surface normal of the confining plates. In the elastic term we took into account all terms up to the second order in Q. Equation (A6) represents the most general expansion of f_s to quadratic order exhibiting tangential isotropic symmetry [29]. Molecular mean-field analysis [29] reveals that $w_1^{(1)}$ includes the direct substrate-LC molecule interactions. On the other hand the remaining surface interaction constants emerge from modification of interactions between LC molecules at the substrate. We set that all the material-dependent quantities introduced in Eqs. (A4)–(A6) are temperature-independent. Furthermore, both confining substrates are assumed to be identical and imposing isotropic tangential anchoring. Key free energy density contributions in the uniaxial nematic phase approximation are expressed in Appendix B.

Dynamics of the system is described by the Euler-Lagrange equation

$$\gamma \frac{\partial Q_{ij}}{\partial t} = -\left[\frac{\delta F}{\delta Q_{ij}} - \frac{1}{3}\mathrm{Tr}\left(\frac{\delta F}{\delta Q_{kl}}\right)\delta_{ij}\right], \tag{A7}$$

where back-flow effects are neglected and γ estimates the effective orientational LC viscosity.

APPENDIX B: UNIAXIAL APPROXIMATION

In the model we used the uniaxial approximation for Q, with a single degenerate eigenvalue S. This simplifies the three energy contribution expressions (A4)–(A6) to

$$f_c(T) = a_0(T - T^*) - bS^3 + cS^4, \tag{B1}$$

$$f_e = \frac{L_0}{2}|\nabla S|^2 + f_e^{(F)}, \tag{B2}$$

$$f_s = -w_1 S + w_2 S^2. \tag{B3}$$

In Eq. (B2), the first term is a contribution that penalizes variations in S, independent of $\mathbf{n}$, while $f_e^{(F)}$ is the classical Frank-Oseen free energy expression, which includes the saddle-splay contributions. In this approximation the influence of planar surfaces Eq. (B3) is independent of the director $\mathbf{n}$, and w_1 and w_2 are positive surface constants according to the molecular mean field analysis, related to the constants of Eq. (A6) as

$$w_1 = \frac{w_1^{(1)}}{3}, \quad w_2 = \frac{2w_1^{(2)}}{3} + \frac{w_2^{(1)}}{9} + \frac{w_2^{(2)}}{9}, \tag{B4}$$

$$K_1 = 2\big(2L_1^{(2)} + L_2^{(2)} + L_3^{(2)} - L_5^{(2)} - 2L_6^{(2)}\big)S^2, \tag{B5}$$

$$K_2 = 4\big(L_1^{(2)} - L_6^{(2)}\big)S^2, \tag{B6}$$

$$K_3 = \big(2L_1^{(2)} + L_2^{(2)} + L_3^{(2)} - L_5^{(2)} - 2L_6^{(2)}\big)S^2, \tag{B7}$$

$$K_{24} = 2L^{(1)}S + 2\left(2L_1^{(2)} + L_3^{(2)} - \frac{1}{3}L_5^{(2)} - 2L_6^{(2)}\right)S^2. \tag{B8}$$

In Eq. (B3) a single elastic constant approximation was used:

$$K = K_i = kS^2, \quad K_{24} = k_{24}^{(1)}S + k_{24}^{(2)}S^2. \tag{B9}$$

APPENDIX C: DOMAINS SIZE IN THE NEMATIC PHASE

We estimate the average size of domains in our samples deep in the nematic phase as a function of the cell thickness and material properties. In our estimate, we implement the Imry-Ma type approach [49] which we adapt to confined nonchiral LCs. We assume that the confining surfaces are a source of a random-field–type disturbance to nematic orientational order. On the other, the volume elasticity favors spatially homogeneous order. The compromised structure between these contradicting tendencies consists of domains of characteristic linear size $\xi_d^{(IM)}$ which we derive below.

We use a minimal model in which we compete the Frank-Oseen bulk elastic and Rapini-Papoular surface anchoring free energy term [42]. The resulting free energy F in the approximation of single Frank elastic constant K reads

$$F \sim \int \frac{K}{2}|\nabla \mathbf{n}|^2 \mathrm{d}^3\mathbf{r} - \int \frac{W(\mathbf{e}\cdot\mathbf{n})^2}{2}\mathrm{d}^2\mathbf{r}. \tag{C1}$$

The positive surface anchoring constant W enforces the director field alignment along the local easy axis $\mathbf{e}$ ($|\mathbf{e}| = 1$).

Random field-type orientational disorder of the surfaces is mimicked by a random distribution of easy axis orientations within the cell limiting substrates at $z = 0$ and $z = h$. In a thin enough cell we assume effective 2D-type behavior, where spatial variations along the z axis are neglected. Following the Imry-Ma argument we set that the system breaks into a domain-type structure, characterized by $\xi_d^{(IM)}$. Therefore, $F \sim N_d F_d$, N_d stands for the number of domains and F_d is the free energy penalty within an average domain:

$$F_d \sim \frac{\xi_d^2}{2}\left(\frac{Kd}{\xi_d^{(IM)^2}} - W\langle g_s\rangle_d\right), \tag{C2}$$

where $\langle\cdot\rangle_d$ stands for the spatial average within the domain and $g_s = (\mathbf{e}\cdot\mathbf{n})^2 - 1/2$. Note that $\langle g_s\rangle_d \to 0$ in a large

TABLE I. Numerical values of parameters used in calculations.

Constant	Value	Units	Name/description
S_0	0.4	—	Equilibrium scalar order parameter
T_{IN}	308.55	K	5CB N-I bulk transition temperature
T^*	307.45	K	5CB bulk supercooling temperature
a_0	6.5×10^4	J/(Km^3)	Leading term constant in Landau expansion
L_0	1.4×10^{-11}	N	Single elastic constant
γ	0.143	Js/m^3	Rotational viscosity
σ_{IN}	1.1×10^{-5}	J/m^2	Isotropic-nematic surface tension
ξ_{IN}	10×10^{-9}	m	Correlation distance at T_{IN}
τ_{IN}	2×10^{-6}	s	Nematic correlation time at T_{IN}
w_1	1.1×10^{-3}	J/m^2	Anchoring related to ordering, determines h_c
w_2	3.85×10^{-3}	J/m^2	Anchoring related to disordering, T shift
$l_e^{(1)}$	5.1×10^{-9}	m	Extrapolation length of the ordering field
$l_e^{(2)}$	3.63×10^{-9}	m	Extrapolation length of the disordering field
h_c	78.6	nm	Critical thickness determined as $h_c = 4\xi_{IN}/(l_e^{(1)})$
$k_B T^*$	4.25×10^{-21}	J	Used thermal energy

enough domain. According to the central limit theorem it holds that $\langle g_s \rangle_d \sim 1/\sqrt{N}$, where $N \sim ((\xi_d^{(IM)}/a_{rf})^{D_{\text{eff}}}$ counts the number of random-field reorientations within the domain, a_{rf} estimates an average distance between nearby "random sites," and $D_{\text{eff}} = 2$ is the effective space dimensionality within which the averaging takes place. We estimate $\xi_d^{(IM)}$ by balancing average and interface penalty conditions (i.e., we impose $F_d = 0$) and obtain

$$\xi_d^{(IM)} \sim \frac{Kd}{Wa_{rf}}. \tag{C3}$$

APPENDIX D: NUMERICAL VALUES

The constants used in our numerical calculations are listed in Table I.

---

[1] W. Thomson, 4. On the equilibrium of vapour at a curved surface of liquid, Proc. R. Soc. Edinburgh **7**, 63 (1872).

[2] L. R. Fisher, R. A. Gamble, and J. Middlehurst, The Kelvin equation and the capillary condensation of water, Nature (London) **290**, 575 (1981).

[3] P. Sheng, Phase transition in surface-aligned nematic films, Phys. Rev. Lett. **37**, 1059 (1976).

[4] P. Sheng, Boundary-layer phase transition in nematic liquid crystals, Phys. Rev. A **26**, 1610 (1982).

[5] A. Poniewierski and T. J. Sluckin, Theory of the nematic-isotropic transition in a restricted geometry, Liq. Cryst. **2**, 281 (1987).

[6] X-l. Wu, W. I. Goldburg, M. X. Liu, and J. Z. Xue, Slow dynamics of isotropic-nematic phase transition in silica gels, Phys. Rev. Lett. **69**, 470 (1992).

[7] G. S. Iannacchione, G. P. Crawford, S. Žumer, J. W. Doane, and D. Finotello, Randomly constrained orientational order in porous glass, Phys. Rev. Lett. **71**, 2595 (1993).

[8] S. Kralj, E. G. Virga, and S. Žumer, Biaxial torus around nematic point defects, Phys. Rev. E **60**, 1858 (1999).

[9] A. B. Bračič, K. Kočevar, I. Muševič, and S. Žumer, Capillary forces in a confined isotropic-nematic liquid crystal, Phys. Rev. E **68**, 011708 (2003).

[10] H. Yokoyama, Nematic–isotropic transition in bounded thin films, J. Chem. Soc. Faraday Trans. 2 **84**, 1023 (1988).

[11] K. Kočevar, A. Borštnik, I. Muševič, and S. Žumer, Capillary condensation of a nematic liquid crystal observed by force spectroscopy, Phys. Rev. Lett. **86**, 5914 (2001).

[12] H. Stark, J. ichi Fukuda, and H. Yokoyama, Capillary condensation in liquid-crystal colloids, Phys. Rev. Lett. **92**, 205502 (2004).

[13] M. M. Wittebrood, T. Rasing, S. Stallinga, and I. Muševič, Confinement effects on the collective excitations in thin nematic films, Phys. Rev. Lett. **80**, 1232 (1998).

[14] M. Rho and I. Zahed, *The Multifaceted Skyrmion* (World Scientific, Singapore, 2016).

[15] X. Zhang, Y. Zhou, K. M. Song, T.-E. Park, J. Xia, M. Ezawa, X. Liu, W. Zhao, G. Zhao, and S. Woo, Skyrmion-electronics: Writing, deleting, reading and processing magnetic skyrmions toward spintronic applications, J. Phys.: Condens. Matter **32**, 143001 (2020).

[16] S.-Z. Lin, A. Saxena, and C. D. Batista, Skyrmion fractionalization and merons in chiral magnets with easy-plane anisotropy, Phys. Rev. B **91**, 224407 (2015).

[17] S. Gao, H. D. Rosales, F. A. G. Albarracín, V. Tsurkan, G. Kaur, T. Fennell, P. Steffens, M. Boehm, P. Čermák, A. Schneidewind, E. Ressouche, D. C. Cabra, C. Rüegg, and O. Zaharko, Fractional antiferromagnetic skyrmion lattice induced by anisotropic couplings, Nature (London) **586**, 37 (2020).

[18] J. Pišljar, S. Ghosh, S. Turlapati, N. Rao, M. Škarabot, A. Mertelj, A. Petelin, A. Nych, M. Marinčič, A. Pusovnik, M. Ravnik, and I. Muševič, Blue phase III: Topological fluid of skyrmions, Phys. Rev. X **12**, 011003 (2022).

[19] J. Pišljar, A. Nych, U. Ognysta, A. Petelin, S. Kralj, and I. Muševič, Dynamics and topology of symmetry breaking with skyrmions, Phys. Rev. Lett. **132**, 178101 (2024).

[20] F. G. Yaremenko, N. S. Pivnenko, L. A. Kutulya, Z. A. Kondratyuk, N. B. Novikova, and N. I. Shkolnikova, New steroid a,b-unsaturated ketones as chiral components of induced cholesteric liquid crystal systems, Russ. Chem. Bull. **58**, 1072 (2009).

[21] J. Li and S.-T. Wu, Extended cauchy equations for the refractive indices of liquid crystals, J. Appl. Phys. **95**, 896 (2004).

[22] See Supplemental Material at http://link.aps.org/supplemental/10.1103/PhysRevE.111.045415 for a list and description of included Supplemental Videos.

[23] I. M. Syed, G. Carbone, C. Rosenblatt, and B. Wen, Planar degenerate substrate for micro- and nanopatterned nematic liquid-crystal cells, J. Appl. Phys. **98**, 034303 (2005).

[24] F. Nemoto, I. Nishiyama, Y. Takanishi, and J. Yamamoto, Anchoring and alignment in a liquid crystal cell: Self-alignment of homogeneous nematic, Soft Matter **8**, 11526 (2012).

[25] A. Nych, J. Fukuda, U. Ognysta, S. Žumer, and I. Muševič, Spontaneous formation and dynamics of half-skyrmions in a chiral liquid-crystal film, Nat. Phys. **13**, 1215 (2017).

[26] D. Allan, C. van der Wel, N. Keim, T. A. Caswell, D. Wieker, R. Verweij, C. Reid, Thierry, L. Grueter, K. Ramos, apiszcz, zoeith, R. W. Perry, F. Boulogne, P. Sinha, pfigliozzi, N. Bruot, L. Uieda, J. Katins, H. Mary *et al.*, soft-matter/trackpy: Trackpy v0.4.2, Zenodo (2019).

[27] M. Kleman, *Soft Matter Physics: An Introduction* (Springer-Verlag, New York, 2004).

[28] T. J. Sluckin and A. Poniewierski, Novel surface phase transition in nematic liquid crystals: Wetting and the Kosterlitz-Thouless transition, Phys. Rev. Lett. **55**, 2907 (1985).

[29] A. K. Sen and D. E. Sullivan, Landau-de Gennes theory of wetting and orientational transitions at a nematic-liquid substrate interface, Phys. Rev. A **35**, 1391 (1987).

[30] S. Kralj, S. Žumer, and D. W. Allender, Nematic-isotropic phase transition in a liquid-crystal droplet, Phys. Rev. A **43**, 2943 (1991).

[31] S. Herminghaus, K. Jacobs, K. Mecke, J. Bischof, A. Fery, M. Ibn-Elhaj, and S. Schlagowski, Spinodal dewetting in liquid crystal and liquid metal films, Science **282**, 916 (1998).

[32] D. van Effenterre, R. Ober, M. P. Valignat, and A. M. Cazabat, Binary separation in very thin nematic films: Thickness and phase coexistence, Phys. Rev. Lett. **87**, 125701 (2001).

[33] M. I. Boamfa, M. W. Kim, J. C. Maan, and T. Rasing, Observation of surface and bulk phase transitions in nematic liquid crystals, Nature (London) **421**, 149 (2003).

[34] S. Aya, Y. Sasaki, F. Araoka, K. Ema, K. Ishikawa, A. V. Emelyanenko, and H. Takezoe, Observation of two isotropic-nematic phase transitions near a surface, Phys. Rev. Lett. **106**, 117801 (2011).

[35] A. V. Emelyanenko, S. Aya, Y. Sasaki, F. Araoka, K. Ema, K. Ishikawa, and H. Takezoe, Two transitions between isotropic and nematic phases in confined liquid crystals, Phys. Rev. E **84**, 041701 (2011).

[36] J. M. Kosterlitz and D. J. Thouless, Ordering, metastability and phase transitions in two-dimensional systems, J. Phys. C **6**, 1181 (1973).

[37] Z. Kutnjak, S. Kralj, G. Lahajnar, and S. Žumer, Calorimetric study of octylcyanobiphenyl liquid crystal confined to a controlled-pore glass, Phys. Rev. E **68**, 021705 (2003).

[38] A. V. Kityk, M. Wolff, K. Knorr, D. Morineau, R. Lefort, and P. Huber, Continuous paranematic-to-nematic ordering transitions of liquid crystals in tubular silica nanochannels, Phys. Rev. Lett. **101**, 187801 (2008).

[39] D. Cleaver, S. Kralj, T. Sluckin, and M. Allen, Liquid crystals in complex geometries formed by polymer and porous networks, in *The Random Anisotropy Nematic Spin Model*, edited by G. Crawford and S. Žumer (Taylor and Francis Group, London, 1996), pp. 467–481.

[40] P. Oswald and G. Poy, Droplet relaxation in Helse-Shaw geometry: Application to the measurement of the nematic-isotropic surface tension, Phys. Rev. E **92**, 062512 (2015).

[41] S. Faetti and V. Palleschi, Measurements of the interfacial tension between nematic and isotropic phase of some cyanobiphenyls, J. Chem. Phys. **81**, 6254 (1984).

[42] P. G. de Gennes and J. Prost, *Physics of Liquid Crystals* (Oxford University Press, Oxford, 1995).

[43] R. Blinc, S. Lugomer, and B. Žekš, Soft-mode dynamics in nematic liquid crystals, Phys. Rev. A **9**, 2214 (1974).

[44] G. Venkataraman, Soft modes and structural phase transitions, Bull. Mater. Sci. **1**, 129 (1979).

[45] G. Schwalb and F. W. Deeg, Pore-size-dependent orientational dynamics of a liquid crystal confined in a porous glass, Phys. Rev. Lett. **74**, 1383 (1995).

[46] K. Kočevar and I. Muševič, Forces in the isotropic phase of a confined nematic liquid crystal 5cb, Phys. Rev. E **64**, 051711 (2001).

[47] M. Nespoulous, C. Blanc, and M. Nobili, Orientational quenched disorder of a nematic liquid crystal, Phys. Rev. Lett. **104**, 097801 (2010).

[48] T. Bellini, N. A. Clark, V. Degiorgio, F. Mantegazza, and G. Natale, Light-scattering measurement of the nematic correlation length in a liquid crystal with quenched disorder, Phys. Rev. E **57**, 2996 (1998).

[49] Y. Imry and S.-K. Ma, Random-field instability of the ordered state of continuous symmetry, Phys. Rev. Lett. **35**, 1399 (1975).

[50] Y. Imry and M. Wortis, Influence of quenched impurities on first-order phase transitions, Phys. Rev. B **19**, 3580 (1979).

[51] S. Jeon, T. Heo, S.-Y. Hwang, J. Ciston, K. C. Bustillo, B. W. Reed, J. Ham, S. Kang, S. Kim, J. Lim, K. Lim, J. S. Kim, M.-H. Kang, R. S. Bloom, S. Hong, K. Kim, A. Zettl, W. Y. Kim, P. Ercius, J. Park *et al.*, Reversible disorder-order transitions in atomic crystal nucleation, Science **371**, 498 (2021).

[52] J. J. D. Yoreo, Principles of crystal nucleation and growth, Rev. Mineral. Geochem. **54**, 57 (2003).

[53] S. Žumer and S. Kralj, Influence of k_{24} on the structure of nematic liquid crystal droplets, Liq. Cryst. **12**, 613 (1992).